JCI insight

Multi-omics characterization of esophageal squamous cell carcinoma identifies molecular subtypes and therapeutic targets

Dengyun Zhao, … , Zigang Dong, Kangdong Liu

JCI Insight. 2024. https://doi.org/10.1172/jci.insight.171916.

Research In-Press Preview Oncology Therapeutics

Graphical abstract

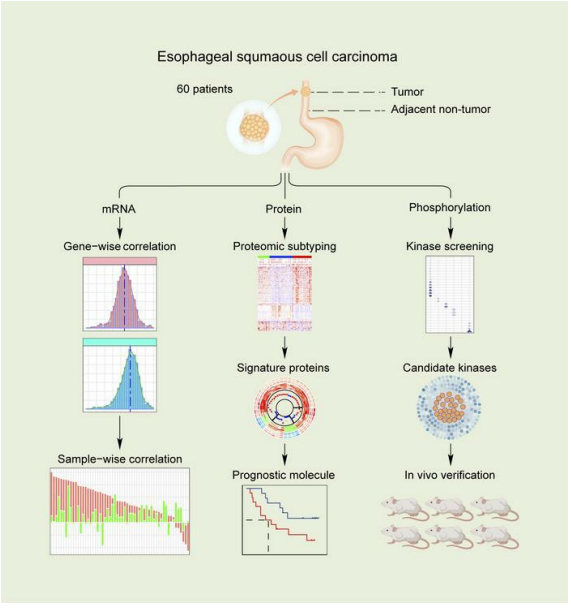

Multi-omics characterization of esophageal squamous cell carcinoma identifies molecular subtypes and therapeutic targets

Dengyun Zhao,[1,2,3] Yaping Guo,[1,4,5] Huifang Wei,[1,2] Xuechao Jia,[1,2] Yafei Zhi,[1,2] Guiliang He,[2] Wenna Nie,[2] Limeng Huang,[2] Penglei Wang,[1,2] Kyle Vaughn Laster,[2] Zhicai Liu,[6] Jinwu Wang,[6] Mee-Hyun Lee,[1,2,7] Zigang Dong,[1,2,3,4,5,8] and Kangdong Liu[1,2,3,4,5,8]

[1]Department of Pathophysiology, School of Basic Medical Sciences, Academy of Medical Sciences，Zhengzhou University, Zhengzhou, Henan, China. [2]China-US (Henan) Hormel Cancer Institute, Zhengzhou, Henan, China. [3]Tianjian Laboratory of Advanced Biomedical Sciences, Zhengzhou, Henan, China. [4]The Collaborative Innovation Center of Henan Province for Cancer Chemoprevention, Zhengzhou, Henan, China. [5]State Key Laboratory of Esophageal Cancer Prevention and Treatment, Zhengzhou University, Zhengzhou, Henan, China. [6]Linzhou Cancer Hospital, Anyang, Henan, China. [7]College of Korean Medicine, Dongshin University, Naju, Jeonnam, Republic of Korea. [8]Provincial Cooperative Innovation Center for Cancer Chemoprevention, Zhengzhou University, Zhengzhou, Henan, China.

Authorship note: DZ and YG contributed equally to this work. MHL, ZD, and KL are co-senior authors.

Conflict of interest: The authors have declared that no conflict of interest exists.

Multi-omics characterization of esophageal squamous cell carcinoma identifies molecular subtypes and therapeutic targets

Abstract

Esophageal squamous cell carcinoma (ESCC) is the predominant form of esophageal cancer and is characterized by an unfavorable prognosis. To elucidate the distinct molecular alterations in ESCC and investigate therapeutic targets, we performed a comprehensive analysis of transcriptomic, proteomic, and phosphoproteomic data derived from 60 paired treatment-naive ESCC and adjacent non-tumor tissue samples. Additionally, we conducted a correlation analysis to describe the regulatory relationship between transcriptomic and proteomic processes, revealing alterations in key metabolic pathways. Unsupervised clustering analysis of the proteomic data stratified ESCC patients into three subtypes with different molecular characteristics and clinical outcomes. Notably, subtype III exhibited the worst prognosis and enrichment in proteins associated with malignant processes, including glycolysis and DNA repair pathways. Furthermore, translocase of inner mitochondrial membrane domain containing 1 (TIMMDC1) was validated as a potential prognostic molecule for ESCC. Moreover, integrated kinase-substrate network analysis using the phosphoproteome nominated candidate kinases as potential targets. In vitro and in vivo experiments further confirmed casein kinase II subunit alpha (CSNK2A1) as a potential kinase target for ESCC. These underlying data represent a valuable resource for researchers, which may provide better insights into the biology and treatment of ESCC.

Introduction

Esophageal cancer is a highly aggressive malignancy and is the sixth most common cause of

cancer-related mortality worldwide (1, 2). Esophageal squamous cell carcinoma (ESCC) and esophageal adenocarcinoma (EAC) are the two main histopathological subtypes of esophageal cancer, among which ESCC accounts for approximately 90% of the diagnosed cases (3). Current therapeutic options for ESCC include endoscopic therapy, surgery, chemotherapy, radiotherapy, and comprehensive treatment. Several studies (4-10) have demonstrated that various inhibitors targeting VEGFR (e.g., apatinib and anlotinib), HER-2 (e.g., lapatinib), and PD-1/PD-L1 (e.g., pembrolizumab, camrelizumab, and toripalimab) can improve the survival rates of patients with ESCC. Currently, pembrolizumab, lapatinib, and anlotinib are approved for the first- or second-line treatment of ESCC (6-8). Despite advancements in treatment strategies, patient clinical outcomes remain unsatisfactory, primarily due to the heterogeneity of individual patients, lack of early specific symptoms, and absence of effective screening strategies, resulting in frequent diagnosis at advanced stages.

In the past decade, large-scale sequencing efforts have been made to investigate the underlying molecular alterations in ESCC. For instance, comprehensive genomic studies (11-13) have revealed that TP53, RB1, CDKN2A, NOTCH1, and FAT1 are the most frequently mutated genes, which has advanced our understanding of the pathogenic mechanisms involved in ESCC. Currently, multi-dimensional ‘‘omics’’ strategies encompassing proteomic and phosphoproteomic profiling in conjunction with other omics analyses have elucidated molecular subtypes and signaling pathways, revealing potential therapeutic targets for diverse cancer types (14-19). In a recent study (20), ESCC was classified into two different molecular subtypes (S1 and S2) based on proteomic data, and three potentially effective drugs were validated for the treatment of patients with the S2 subtype. However, a comprehensive

phosphoproteomic analysis was not conducted due to the small sample size (n=31 tissue pairs). In another study (21) involving 94 tumor and 24 non-tumor tissue samples, three distinct ESCC subtypes (Subtypes I-III) were identified and the therapeutic potential of TG003, a CLK inhibitor, was confirmed specifically for patients with subtype III. These investigations have enhanced our understanding of ESCC pathogenesis and potential therapeutic strategies for ESCC. However, ESCC patient-paired cohorts with more extensive survival data are needed to further elucidate the molecular alterations contributing to ESCC initiation and development.

In this study, we performed a comprehensive transcriptomic, proteomic, and phosphoproteomic analysis of treatment-naive ESCC and paired adjacent non-tumor tissue samples obtained from 60 patients over a 7-year follow-up period. A correlation analysis between transcriptomic and proteomic data was conducted, revealing alterations in key metabolic pathways. Unsupervised clustering of the proteome identified three subtypes (S-I, S-II, and S-III) associated with different clinical and molecular features. Moreover, integrated kinase substrate network analysis based on the phosphoproteome predicted potential kinase targets which was further verified in experiments. In summary, our study provides complementary information on ESCC, which may contribute to a better understanding of this disease and the development of more effective treatment strategies.

Results

Multi-omic landscape of ESCC samples. In the present study, paired tumor and adjacent non-tumor samples were collected from 60 treatment-naive Chinese patients with ESCC. The samples represented diverse clinical and pathological characteristics including age, sex, and tumor grade and stage. Notably, the 7-year follow-up information was also recorded (Figure 1,

A and B, and Supplemental Table 1). For all 60 paired samples, mRNA sequencing (RNA-seq) and the tandem mass tag (TMT)-based isobaric labeling strategy were employed for precise relative quantification of global mRNAs, proteins, and phosphosites (Figure 1C and Supplemental Figure 1, A and B). At the transcriptional level, a total of 19,615 RNAs were quantified (Supplemental Figure 1C and Supplemental Table 2). TMT-based proteomic and phosphoproteomic analyses revealed a total of 100,898 non-phosphorylated peptides and 28,853 phosphopeptides, the majority of which exhibited two or more spectral counts (Figure 1D). Subsequently, all non-phosphorylated peptides were aligned to their corresponding protein sequences, resulting in mapping to 9,261 proteins, of which 8,224 were quantifiable, and only a minority were mapped to one peptide (Figure 1E). Among the 28,853 identified phosphopeptides, there were 22,611 p-Ser (78%), 5,753 p-Thr (20%), and 489 p-Tyr (2%) peptides, most of which had a localization probability > 0.75 (Figure 1F). In total, we identified 18,944 phosphosites on 5,213 phosphoproteins with a confident site localization score (localization probability >0.75) (Figure 1G). Principal component analysis (PCA) based on the proteomics data revealed no discernible batch effect among the TMT plexes (Supplemental Figure 1D), and the relative quantification information is illustrated in Supplemental Figure 1E. The ESTIMATE analysis of RNA-seq data revealed a higher immune cell infiltration in adjacent non-tumor samples (Supplemental Table 2). The results presented herein demonstrate the high quality of both the samples and the data.

Correlation analysis of transcriptomic and proteomic data. To characterize the relationship between transcriptomic and proteomic processes in ESCC, gene-wise (inter-sample) and sample-wise (intra-sample) correlations of 5,676 mRNA-protein pairs from 57 tumor and 60

adjacent non-tumor tissues were calculated (Methods). The median correlation coefficient for adjacent non-tumor tissues was 0.11, while that for tumor tissues was 0.30 (Figure 2A). The adjacent non-tumor and tumor tissues of ESCC exhibited significant positive Spearman correlation coefficients of 14.98% and 40.15%, respectively, for mRNA-protein pairs (Spearman's correlation, *P* value < 0.01). The enrichment analysis indicated alterations in key metabolic pathways, including xenobiotics by cytochrome p450 metabolism, pyruvate metabolism, glutathione metabolism, and glycolysis gluconeogenesis (Figure 2A). Additionally, the sample-wise mRNA-protein correlation analysis revealed a higher correlation value in tumor tissues than in adjacent non-tumor tissues (Figure 2B and Supplemental Table 3).

Proteomic features of tumor tissues compared to adjacent non-tumor tissues. Given that proteins serve as crucial functional executors within cells, we performed an in-depth proteomic analysis. The proteome-based correlation analysis demonstrated decreased correlations in tumors compared to adjacent non-tumors, suggesting high individual tumor heterogeneity in ESCC (Supplemental Figure 2A). Moreover, we identified 751 upregulated and 274 downregulated proteins in tumor tissues compared to adjacent non-tumor tissues among the 8,224 quantified proteins (Figure 2C and Supplemental Table 2). KEGG pathway enrichment analysis revealed that the upregulated proteins were enriched in DNA replication, spliceosome, and antigen processing and presentation, while the downregulated proteins were enriched in protein digestion and absorption, cell adhesion, PPAR signaling pathway, and arachidonic acid metabolism pathway (Figure 2D). In addition, our enrichment analysis based on cancer hallmark gene sets from the Molecular Signatures Database (MsigDB) revealed substantial involvement of these dysregulated proteins in malignancy-associated pathways, including

epithelial-mesenchymal transition (EMT), E2F targets, G2/M checkpoint, and mTORC1 signaling pathway (Supplemental Figure 2B).

We also identified a series of proteins associated with cancer development that have been previously reported. Specifically, the protein levels of genes frequently mutated in ESCC were found to be upregulated, including CDKN2A, CHEK1, EGFR, RB1, and TP53 (12). Other notable proteins, such as ACKR3, COL11A1, CPA4, and FZD6, were previously reported (22-25) as potential therapeutic targets in cancer. Moreover, previous studies (26-32) have implicated ACKR3, CHAF1B, CHEK1, and COL11A1 are involved in cancer cell proliferation, while CA9, CHAF1B, and COL11A1 play roles in cancer invasion and migration (Figure 2E). These findings provide valuable insights for understanding the biology of ESCC. In addition, subcellular localization analysis revealed that the differentially regulated proteins were predominantly localized in the nucleus, cytoplasm, and plasma membrane (Supplemental Figure 2C).

Protein abundance-based subtyping of ESCC. PCA analysis based on the proteomics data indicated a clear boundary between tumor and adjacent non-tumor tissues (Figure 3A). By employing unsupervised consensus clustering analysis, we identified three subtypes (S-I, S-II, and S-III) based on the differentially expressed proteins (Figure 3B and Supplemental Figure 3, A and B). To explore potential associations between clinicopathological characteristics and these three subtypes, we evaluated TNM stage and occurrence of lymphatic metastasis in each patient based on subtype. Interestingly, the incidence of lymphatic metastasis was higher in the S-II (46.2%) and S-III subtypes (47.6%) compared to the S-I subtype (23.1%). Additionally, a greater proportion of patients diagnosed with stage III were observed in S-II (61.5%) and S-III

subtypes (71.4%) compared to the S-I subtype (53.8%) (Figure 3B). Further analysis demonstrated that patients with the S-I subtype had the best prognosis, whereas patients with the S-III subtype had the worst prognosis (Log-rank test, P = 0.036) (Figure 3C). Enrichment analysis demonstrated that metabolism-related processes such as fatty acid metabolism, adipogenesis, and reactive oxygen species were exclusively dysregulated in S-I subtype tumors, demonstrating the metabolic disorder characteristics of these tumors. The Hedgehog signaling pathway, apical junction pathway, and coagulation pathway were found to be enriched within tumors classified as the S-II subtype. In contrast, the glycolysis pathway, DNA repair process, Myc, and cell cycle pathways were enriched within tumors categorized as the S-III subtype, suggesting the proliferative characteristics of these tumors (Figure 3D).

Moreover, integrative molecular network analysis further revealed that, in contrast to the S-I and S-II subtypes, the S-III subtype exhibited aggressive characteristics, including the upregulation of proteins involved in pathways associated with spliceosome (such as SNRPF, PRPF19, and SRSF6) and cell cycle (such as PCNA, MCM2, and MCM4) (Figure 3E and Supplemental Table 4). These findings are consistent with a previous study (20), which suggested that cell cycle and spliceosome-related proteins play crucial roles in ESCC tumorigenesis. Additionally, previous studies reported (12, 33-38) that ESCC-associated proteins, including PCNA, SLC7A5, CTTN, RB1, EGFR, TP63, and PRMT1, exhibited increased expression in the S-III subtype; among these proteins, SLC7A5 and EGFR were FDA-approved drug targets for cancer treatment (Figure 3F). Cox regression analysis was subsequently performed to assess the potential prognostic molecules in the S-III subtype. A series of proteins, including GAR1, PRKDC, SRSF9, SRSF6, SFPQ, RB1, TP63, and

TIMMDC1, were associated with a high prognosis risk score; among those proteins, PRKDC, RB1, and TP63 have been previously reported (39) in ESCC (Figure 3G). Based on the four criteria described in the methods, we nominated TIMMDC1 (Wilcoxon test, P = 3e-13; Log-rank test, *P* = 0.041) as a potential prognostic molecule for further investigation (Supplemental Figure 3, C and D).

Upregulated TIMMDC1 predicts poor prognosis and promotes ESCC development. TIMMDC1, a crucial factor for the assembly of OXPHOS complex I, plays an important role in cellular energy homeostasis under stress conditions (40, 41). A previous study (42) demonstrated that increased levels of TIMMDC1 can promote gastric cancer proliferation. To explore the role of TIMMDC1 in ESCC, we evaluated its expression in a human ESCC tissue microarray (TMA) cohort by immunohistochemistry (IHC) staining. Consistent with our proteomic analysis shown in Supplemental Figure 3C, we observed significant upregulation of TIMMDC1 in tumor tissues compared to non-tumor tissues (Figure 4, A-C). Furthermore, a Kaplan-Meier analysis demonstrated that patients with elevated TIMMDC1 expression had significantly shorter cancer-related survival times than those with low TIMMDC1 expression in the TMA cohort (Log-rank test, *P* = 0.0094) (Figure 4D). Moreover, analysis of RNA-seq data from the TCGA-ESCA cohort revealed significantly increased TIMMDC1 transcript levels in tumor tissues (*P* < 0.0001) (Figure 4E). TIMMDC1 protein levels were determined by Western blotting in paired ESCC and non-tumor tissues, as well as in different ESCC cell lines. Elevated TIMMDC1 protein levels were observed in most tumor tissues compared to non-tumor tissues (Supplemental Figure 4A). In addition, TIMMDC1 was upregulated in ESCC cell lines compared

to the human immortalized normal esophageal epithelial cell line (SHEE) (Supplemental Figure 4B). These findings suggest that TIMMDC1 is a potential prognostic molecule in ESCC.

To investigate the molecular function of TIMMDC1 in ESCC, two specific shTIMMDC1 sequences were designed to knockdown TIMMDC1 in the KYSE30 and KYSE450 cell lines, which express relatively high levels of TIMMDC1 (Supplemental Figure 4B). TIMMDC1 protein levels were decreased in shTIMMDC1 cells compared to scramble cells (Figure 4F). Subsequently, MTT, soft agar, and colony formation assays were performed to assess the impact of TIMMDC1 knockdown on ESCC cell proliferation and colony formation. Our findings demonstrated that knockdown of TIMMDC1 resulted in decreased cell proliferation and suppressed colony formation (Figure 4, G and H, and Supplemental Figure 4, C and D). Furthermore, we investigated whether the overexpression of TIMMDC1 could enhance cell proliferation and colony formation in KYSE70 and KYSE150 cells with relatively low levels of TIMMDC1 expression (Supplemental Figure 4B and Figure 4I). As expected, TIMMDC1 overexpression promoted cell proliferation and colony formation (Figure 4, J and K, and Supplemental Figure 4, E and F). To evaluate the effect of TIMMDC1 on tumor growth in vivo, a cell-derived xenograft (CDX) model was established. Our results demonstrated that TIMMDC1 knockdown inhibited tumor growth and reduced tumor weights compared to those in the scramble group (Figure 4, L-O). In summary, these results provide evidence to support the potential of TIMMDC1 as a promising prognostic and therapeutic molecule for ESCC.

Identification of potentially activated protein kinases. A total of 3,368 phosphoproteins were quantified after normalization of the proteomic and phosphoproteomic data. Among the quantified proteins, we identified 1,113 phosphosites on 689 proteins that were upregulated in

tumor tissues; on the other hand, 606 phosphosites on 441 proteins were downregulated (Supplemental Table 2, Supplemental Figure 5A). Enrichment analysis based on differentially expressed phosphoproteins revealed that the upregulated phosphoproteins showed enrichment mainly in pathways related to Notch signaling, RNA transport, spliceosome, adhesion junction, and cell cycle. Moreover, the downregulated phosphoproteins showed enrichment mainly in pathways associated with spliceosome, tight junction, adhesion junction, and regulation of actin cytoskeleton (Supplemental Figure 5B and Supplemental Table 5). To elucidate the disparities in phosphoproteomic profiles among the patients' proteomic subtypes, we integrated the phosphoproteomic data into our proteomic subtyping analysis. We observed substantial variations in the abundance of quantified phosphosites across the three subtypes (Supplemental Figure 5C). For instance, TP53BP1 is involved in DNA double-strand break repair, and our results revealed that TP53BP1 S1678 exhibited the highest level in the S-III subtype (S-I vs. S-II, *t* test, $P = 0.0062$; S-I vs. S-III, *t* test, $P = 0.05$; S-II vs. S- III, *t* test, $P = 7e\text{-}05$). This finding aligns with our protein subtype analysis, which identified DNA repair as one of the pathways represented in the S-III subtype. Moreover, a previous study (43) reported that CDK1-dependent phosphorylation of TP53BP1 at S1678 impairs its binding to importin during mitosis. Additionally, it has been reported (44) that CK2-dependent phosphorylation of PAK1 at S223 necessitates its catalytically active monomeric form. Our analysis revealed that PAK1 S223 exhibited the highest level in the S-III subtype and the lowest in the S-I subtype (S-I vs. S-II, *t* test, $P = 0.28$; S-I vs. S-III, *t* test, $P = 4.6e\text{-}04$; S-II vs. S-III, *t* test, $P = 0.0021$). Furthermore, we discovered several phosphoproteins associated with the three subtypes, including MAP2, MABPP1A, and PGM5 (Supplemental Figure 5C).

To predict candidate kinases associated with altered phosphorylation networks in ESCC, we performed kinase activity analysis using the iKAP algorithm (45). Our analysis suggested that a total of 28 activated kinases were closely linked to the altered phosphorylation networks (Figure 5, A and B, and Supplemental Table 6). Among these activated kinases, mTOR, CLK1 and CDK7 have been previously reported (21, 46, 47) in ESCC. To investigate the roles of these kinases in ESCC cell proliferation, we generated KYSE30 and KYSE450 knockdown cells with shRNAs that targeted candidate kinases separately. Our results revealed that depletion of the majority of kinase transcripts significantly impaired cell proliferation (Figure 5C and Supplemental Figure 5D). Notably, knockdown of CSNK2A1 resulted in the most pronounced inhibition of cell proliferation in both cell lines. CSNK2A1, a catalytic subunit of CK2, has been identified as a potential therapeutic target in acute myeloid leukemia (48, 49). Therefore, we conducted MTT, soft agar, and colony formation assays to determine the impact of CSNK2A1 knockdown or overexpression on ESCC cell proliferation. The efficiency of CSNK2A1 knockdown and overexpression was confirmed by Western blotting (Supplemental Figure 5, E and G). Our findings revealed that knockdown of CSNK2A1 dramatically reduced the growth of KYSE30 and KYSE450 cells (Figure 5, D and E, and Supplemental Figure 5F), while overexpression of CSNK2A1 promoted the growth of KYSE70 and KYSE150 cells (Figure 5, F and G, and Supplemental Figure 5H). To investigate whether CSNK2A1 contributes to ESCC tumor growth in vivo, a CDX model was also established. Our results demonstrated that depletion of CSNK2A1 profoundly impeded tumor growth in vivo (Figure 5, H-K). Collectively, these findings highlight the potential of CSNK2A1 as a therapeutic target for ESCC.

Histone deacetylase 1 (HDAC1) is a nuclear enzyme involved in transcriptional repression,

and the phosphorylation of HDAC1 at Ser421 and Ser423 by CK2 plays a crucial role in regulating enzymatic activity, complex formation, and transcriptional repression (50). To validate our kinase prediction results, we performed Western blotting on ESCC tissue samples to assess the levels of p-HDAC1 S421/S423. In consistent with our sequencing data, we found elevated level of p-HDAC1 S421/S423 in tumor tissues. These results suggest that CSNK2A1 may initiate downstream substrate phosphorylation events, as visualized within the kinase-substrate network (Supplemental Figure 6A and Figure 5B). We also observed that knockdown of HDAC1 inhibited the cell proliferation of KYSE30 and KYSE450 cells (Supplemental Figure 6, B-D). To investigate the function of the p-HDAC1 S421/S423 sites, we generated phosphorylation-deficient double mutants (denoted as HDAC1 S421/S423A) and phosphorylation-mimetic double mutants (denoted as HDAC1 S421/S423D) in KYSE70 and KYSE150 cells. MTT and colony formation assays revealed that HDAC1 S421/S423A mutant cells exhibited lower proliferation and colony formation abilities than HDAC1-WT and HDAC1 S421/S423D mutant cells (Supplemental Figure 6, E and F). Subsequently, we investigated the impact of HDAC1 S421/S423 phosphorylation on HDAC1 enzymatic activity. Our results revealed that HDAC1-S421/S423A mutant cells exhibited decreased HDAC1 enzymatic activity compared to that of HDAC1-WT and HDAC1-S421/S423D mutant cells (Supplemental Figure 6G). It has been reported (48) that EGFR-mediated activation of ERK2 can facilitate the phosphorylation of CK2 at T360/S362 and thus enhance CK2 activity. To explore the function of the CSNK2A1 T360/S362 sites in regulating HDAC1 activity, we generated CSNK2A1 S421/S423A and CSNK2A1 S421/S423D mutant cells. In vitro kinase assay results indicated that the CSNK2A1 S421/S423 sites play a crucial role in activating HDAC1 (Supplemental

Figure 6H). Furthermore, we found that compared to CSNK2A1-WT and CSNK2A1 S421/S423D mutant, CSNK2A1 S421/S423A suppressed cell proliferation and colony formation abilities (Supplemental Figure 6, I and J).

To further elucidate the molecular function of CSNK2A1 in ESCC, we conducted a comparative analysis of protein expression between the high and low CSNK2A1 expression groups (Supplemental Figure 7A). Furthermore, enrichment analysis revealed that crucial pathways involved in cell proliferation, including DNA replication and cell cycle, were enriched in the group with high CSNK2A1 expression (Supplemental Figure 7B and Supplemental Table 7). In the CSNK2A1 high expression group, we noted several highly expressed proteins that have been previously implicated (34, 51-53) in ESCC development, including IGFBP3 (Wilcoxon test, P = 0.014), LAMC2 (Wilcoxon test, P = 0.0042), MAGEA4 (Wilcoxon test, P = 0.05), and SLC7A5 (Wilcoxon test, P = 7.9e-04) (Supplemental Figure 7C). Additionally, we found some proteins in the CSNK2A1 high expression group were correlated with patient survival, including CPOX (Wilcoxon test, P = 2.2e-06; Log-rank test, P = 0.0017), DSC3 (Wilcoxon test, P = 2.6e-04; Log-rank test, P = 0.071), PKP1 (Wilcoxon test, P = 6.9e-06; Log-rank test, P = 0.042), and RPLP1 (Wilcoxon test, P = 0.0016; Log-rank test, P = 0.047) (Supplemental Figure 7D).

Inhibitory effect of CSNK2A1 in vitro and in vivo. Silmitasertib (CX-4945) is a potent and orally bioavailable CK2 inhibitor with broad-spectrum anti-cancer activity (54). Clinical trials have been conducted to evaluate the efficacy of CX-4945 in the treatment of cholangiocarcinoma (NCT02128282), COVID-19 (NCT04663737), coronavirus (NCT04668209), and other diseases. To investigate the potential therapeutic effects of targeting

CSNK2A1 with CX-4945 on ESCC cell growth, we performed MTT, soft agar, and organoid culture assays. CX-4945 effectively inhibited cell proliferation and organoid growth in a dose-dependent manner (Figure 6, A-C, and Supplemental Figure 8, A-C). Subsequently, we examined whether the effect of CX-4945 on ESCC growth was dependent on the levels of CSNK2A1 or p-CSNK2A1 T360/S362. We analyzed the correlation between CSNK2A1 or p-CSNK2A1 T360/S362 levels and the inhibition rates of cell proliferation (Figure 6, D and E). The results demonstrated that ESCC cells with high p-CSNK2A1 T360/S362 levels were more sensitive to CX-4945 treatment (Figure 6F). Furthermore, we evaluated the therapeutic efficacy of CX-4945 using ESCC patient-derived xenograft (PDX) mice models derived from LEG379, LEG397, and LEG460 cases with relatively elevated or moderate p-CSNK2A1 T360/S362 levels (Supplemental Figure 8, D and E). Our results demonstrated that the tumor volumes (Figure 6, G and H) and weights (Figure 6, I and J) of the LEG379 tumors decreased upon CX-4945 treatment. Similarly, CX-4945 treatment also inhibited LEG397 and LEG460 tumor growth (Figure 6, K-N, and Supplemental Figure 8, F-I).

To elucidate the specific contribution of CSNK2A1 to tumor growth, we conducted an in vivo knockdown experiment using LEG244 PDX model mice by employing lentivirus-mediated shRNA delivery targeting CSNK2A1 (Supplemental Figure 8E). Our results demonstrated a reduction in tumor volumes and weights upon knockdown of CSNK2A1 compared to those in the scramble group, resulting in an approximately 60% suppression rate (Figure 6, O-R). To further validate the impact of p-CSNK2A1 T360/S362 on tumor growth in ESCC, we measured expression and phosphorylation levels of CSNK2A1 and HDAC1 in tumor samples obtained from our PDX models by Western blotting. Our results indicated that CX-4945 treatment or

CSNK2A1 knockdown led to a reduction of p-CSNK2A1 T360/S362 and p-HDAC1 S421/S423 levels in these PDX models (Supplemental Figure 8J). In summary, these findings underscore the potential importance of targeting CSNK2A1 for ESCC treatment.

Discussion

In this study, we conducted a comprehensive omics analysis that revealed the molecular alterations in ESCC and identified potential prognostic molecules and therapeutic targets. Despite substantial advancements achieved through large-scale omics profiling of ESCC, previous phosphoproteomic analyses were limited by sample scarcity (20, 21, 55). We overcame this limitation in our research by utilizing a larger number of paired patient tissues to generate transcriptomic, proteomic, and phosphoproteomic datasets. In our study, correlations between transcriptomic and proteomic data were investigated, revealing alterations in various key metabolic pathways. Clustering analysis of the proteomic data revealed three distinct molecular subtypes of ESCC. Subsequent analysis of these subtypes revealed TIMMDC1 as a potential prognostic molecule for ESCC. Additionally, the phosphoproteomic analysis highlighted CSNK2A1 as a potential therapeutic target for ESCC.

Determining the correlations between mRNA and protein products has facilitated the investigation of downstream signaling consequences resulting from genetic alterations in various cancers (14, 15, 18, 56-61). Our analysis revealed a more robust gene-wise and sample-wise correlations in tumor tissues than in non-tumor tissues. Moreover, our observations indicate that the key pathways altered in ESCC predominantly involve in metabolic processes. Additionally, our analysis revealed that the differentially expressed proteins showed enrichment in pathways related to DNA replication, spliceosome, and immune-related signaling

pathways. These findings are consistent with previous studies (20, 62) on esophageal and gastric cancer. Moreover, the functions of some differentially expressed proteins identified in our study have been previously investigated (46, 63-68), several EMT-related proteins, such as WNT5A, MMP1, MMP2, MMP14, LAMC2, FN1, and COL5A2, have been found to enhance cancer cell migration and invasion, suggesting their potential involvement in metastasis. Furthermore, certain cell cycle-related proteins, including TOP2A, PCNA, MCM2, MCM4, MCM5, MCM6, and MCM7, have also been reported (69-71) to facilitate cancer cell proliferation, and the enhanced expression of these cell cycle-related proteins may contribute to uncontrolled ESCC cell proliferation. Collectively, these transcriptomic and proteomic analyses provide valuable insights into the molecular alterations underlying ESCC progression.

Molecular subtyping of cancers can aid patient stratification based on precise molecular signatures to achieve personalized diagnosis and treatment planning. Currently, liquid chromatography-tandem mass spectrometry (LC-MS/MS) proteomics data have been utilized in several studies (57, 60, 62, 72-77) to perform molecular subtyping of various cancer types, including gastric cancer, lung cancer, early-stage hepatocellular carcinoma, head and neck squamous cell carcinoma, pancreatic ductal adenocarcinoma, colorectal cancer, and breast cancer. Additionally, molecular subtyping of ESCC patient-derived tissue samples has been performed based on gene mutation and transcription profiling data (78, 79). Our proteomic analysis classified 60 patient tissue samples into three distinct subtypes. Among these subtypes, patients with the S-III subtype exhibited the poorest survival outcome. Notably, a study (21) conducted by Li *et al*. also classified patients into three subtypes; however, their follow-up period (approximately 2 years) was shorter than that of our study (7 years). Therefore,

we considered that our protein-based subtype classification using a longer follow-up period more accurately reflects the clinical status of patients and provides better guidance for treatment decisions. Consistent with previous investigations (20, 21), we found that the cell cycle, E2F targets, EMT, and spliceosome-related pathways were important for maintaining the ESCC phenotype. Furthermore, our analysis revealed that the S-I subtype exhibited enrichment of proteins involved in fatty acid metabolism, adipogenesis, and reactive oxygen species. The S-II subtype showed enrichment of proteins associated with Hedgehog signaling, apical junction, and coagulation. Moreover, the S-III subtype was characterized by an enrichment of proteins involved in glycolysis and DNA repair. Additionally, we discovered several actionable protein targets within three subtypes, such as SPARC, COL1A1, ADH1B, L1CAM, S100A7, PCNA, and EGFR. These targets can be effectively modulated using FDA-approved drugs. Furthermore, ongoing investigations are exploring the potential of MMP14, CASP7, and PRMT1 as candidate drug targets (80). Collectively, these findings provide complementary information regarding the molecular subtypes of ESCC and their potential clinical implications for future therapeutic interventions.

A previous study (81) reported that TIMMDC1 interacts with multiple members of the mitochondrial complex I assembly factor family and core complex I subunits. Inhibition of TIMMDC1 in HeLa cells resulted in decreased cellular respiration, complex I activity, and complex I subunit stability (40). Additionally, depletion of TIMMDC1 inhibited migration and proliferation in 95D lung carcinoma cells, leading to a marked reduction in mitochondrial viability, membrane potential, and ATPase activity within these cells (82). Moreover, researchers have observed that tumor growth is inhibited due to impaired efficiency of the electron transport chain

and oxidative mitochondrial metabolism facilitated by complex I (83). Another study (84) suggested that metformin can suppress tumor growth by inhibiting cellular respiration and mitochondrial complex activity. Our study revealed a significant association between elevated levels of TIMMDC1 and poor prognosis. Moreover, knockdown of TIMMDC1 led to inhibition of cell growth both in vitro and in vivo. These experimental findings validate the prognostic value of TIMMDC1 and suggest its potential as a therapeutic target for ESCC.

A key finding of this study is the identification of pivotal kinases with therapeutic potential for ESCC. We selected 28 candidate kinases for experimental perturbation to determine their contributions to ESCC cell proliferation. Among the identified kinase candidates, mTOR, CLK1, and CDK7 have been previously implicated (21, 46, 47) in ESCC development. Our study revealed that inhibition of CSNK2A1 attenuated cell proliferation and suppressed ESCC tumor growth in vivo. Previous studies (85-89) have demonstrated that CSNK2A1 promotes tumorigenesis by enhancing several oncogenic signaling pathways in various malignancies, including breast cancer, lung cancer, kidney cancer, colorectal cancer, and prostate cancer. Additionally, CSNK2A1 promotes the invasion and migration of cells by regulating the EMT, NF-κB, and PI3K-Akt-mTOR signaling pathways (90). Our data analysis revealed proteins associated with elevated CSNK2A1 levels in ESCC that were also correlated with tumor maintenance in other cancer types. For instance, CPOX autoantibodies were identified as discriminatory marker between prostate cancer and healthy tissues (91). DSC3 was identified as a highly specific marker for squamous cell carcinoma (92). Moreover, DSC3 was downregulated in colorectal cancer cells, and its methylation status was shown to be an effective prognostic marker (93). Moreover, CX-4945 is the first CK2-specific inhibitor under

clinical evaluation for its efficacy against human solid and hematological tumors (54). Our findings indicated that CX-4945 exhibits inhibitory effects on ESCC both in vivo and in vitro, suggesting the potential of CSNK2A1 as a promising therapeutic target.

There are several limitations in our study. Firstly, our cohort consisted of only 60 paired clinical samples, a larger clinical cohort would be more conducive to illustrating the molecular characteristics of ESCC. Secondly, although we predicted several proteins as potential prognostic molecules, we validated only one protein (TIMMDC1) from the candidate list. Other proteins may also serve as effective prognostic molecules of ESCC. Regarding TIMMDC1, we have only validated its prognostic potential in a limited number of tissue samples; therefore, more studies using larger sample sizes are necessary to explore its clinical relevance and elucidate the underlying molecular mechanisms. Finally, although our method successfully predicted several kinases, among which CSNK2A1 exhibited a superior inhibitory effect on tumor growth, it is worth considering the utilization of CK2-related drugs for functional verification in future studies on ESCC using additional PDX models, given their ongoing clinical investigation.

In summary, the multi-omics integrative analysis represents a valuable and potent tool that offers a complementary and comprehensive understanding of ESCC, thereby providing an opportunity to facilitate the translation of fundamental research into more precise diagnostic methods and effective treatments.

Methods

Sex as a biological variant. For studies involving humans and animal models, sex was not considered as a biological variable.

Patient samples. The clinical samples used in this multi-omics study were collected from patients at Lin Zhou Cancer Hospital between December 2013 and September 2014. Tumor specimens along with their corresponding adjacent non-tumor tissue samples (defined as those located more than 5 cm away from the tumor margin) were obtained. No preoperative therapy was administered to any of the patients in our cohort. Fresh tissues obtained from surgery were divided into three sections: the first section was fixed with formalin for H&E staining; the second section was treated with RNA stabilization solution, stored at -80°C, and utilized for RNA extraction; and the third section was immediately frozen in liquid nitrogen for 1 hour and subsequently stored at -80°C until protein extraction. Each sample was assigned a unique identification code according to its original record number. Formalin-fixed and paraffin-embedded specimens were generated for each tissue, while the HE-stained slides were independently evaluated by two experienced pathologists who provided information regarding tumor purity, TNM stage, pathological type, and lymphatic status. Patient details, including surgery date, age, sex, smoking history, drinking history, and family history, were recorded. Annual follow-up examinations were performed over a period of seven years.

The TIMMDC1 and p-HDAC1 S421/S423 protein levels were measured in additional ESCC tissues and their corresponding adjacent non-tumor tissues, which were freshly collected at Lin Zhou Cancer Hospital using the same methodology as described above.

Cell lines. The human ESCC cell lines KYSE30, KYSE70, KYSE140, KYSE150, KYSE410, KYSE450, and KYSE510 were obtained from the Type Culture Collection of the Chinese Academy of Sciences (Shanghai, China). The human immortalized normal esophageal epithelial cell line (Shantou human embryonic esophageal cell line, SHEE) was donated by Dr.

Enmin Li from the Laboratory of Tumor Pathology (Shantou University Medical College, Shantou, China). 293T cells were acquired from the American Type Culture Collection (ATCC). All cell lines used in this study were cytogenetically tested. Human ESCC cells were cultured in RPMI-1640 medium supplemented with penicillin (100 units/mL), streptomycin (100 μg/mL), and 10% FBS (Biological Industries, Kibbutz Beit-Haemek, Israel). 293T cells were maintained in DMEM medium supplemented with 10% FBS. All cells were kept at 37°C in an incubator containing 5% CO_2.

Reagents and antibodies. CX-4945 was purchased from Lollane Biotechnology, Shanghai. The antibodies used in this study included: anti-TIMMDC1 (ABclonal, A15839); anti-CSNK2A1 (Proteintech, 10992-1-AP); anti-HDAC1 (Proteintech, 10197-1-AP); anti-p-CSNK2A1 T360/S362 (ABclonal, AP0335); anti-p-HDAC1 S421/S423 (Thermo, PA5-36911); and anti-GAPDH (Proteintech, HRP-60004).

Details for RNA-seq and LC-MS/MS are described in the Supplemental Methods.

Pathway enrichment analysis. The two-sided hypergeometric test was adopted for the KEGG pathway enrichment analysis of differentially expressed proteins or phosphoproteins. For each type, we defined the following:

N = number of human proteins annotated by at least one term

n = number of human proteins annotated by term t

M = number of upregulated or downregulated proteins annotated by at least one term

m = number of upregulated or downregulated proteins annotated by term t

The enrichment ratio was then computed and the *P* value was calculated based on the hypergeometric distribution as follows:

$$Enrichment\ \ ratio = \frac{\frac{m}{M}}{\frac{n}{N}}$$

$$P - value = \sum_{m'=m}^{n} \frac{\binom{M}{m'}\binom{N-M}{n-m'}}{\binom{N}{n}} (Enrichment\ \ ratio \geq 1),$$

or

$$P - value = \sum_{m'=0}^{m} \frac{\binom{M}{m'}\binom{N-M}{n-m'}}{\binom{N}{n}} (Enrichment\ \ ratio < 1)$$

Furthermore, we performed single-sample gene set variation analysis (ssGSEA) using 50 cancer hallmark gene sets collected from the MSigDB to identify the pathway alterations in each subtype. The protein expression matrix was utilized to calculate the ssGSEA scores for each gene set. Normalized enrichment scores (NES) and *P* values were calculated using 1,000 permutations. At least one subtype with an adjusted *P* value < 0.01 was regarded as significantly enriched, and the average NES value was then calculated as the enrichment score (ES) of the proteomic subtypes (94).

Consensus clustering analyses. Prior to clustering analysis, differentially expressed proteins were identified. To identify proteomic subtypes of ESCC, consensus clustering (R package ConsensusClusterPlus version. 1.54.0), a reconciling clustering algorithm with a resampling strategy, was implemented. The basic parameters were set as follows: max up to 6 subtypes (maxK = 6), 5,000-time repetitions (reps = 5,000), and resampling 95% of the samples (pItem = 0.95). Three clustering algorithms with corresponding distance functions were used to obtain the potential subtypes that were significantly associated with overall survival (OS) outcomes. In the k-means (KM) clustering, Euclidean distance was applied; in the hierarchical clustering

(HC) and partitioning around the medoid (PAM), 7 distance functions comprising Pearson (1 - Pearson correlation), Spearman (1 - Spearman correlation), Euclidean, binary, maximum, Canberra, and Minkowski was applied. Finally, the optimal subtype for proteins and the corresponding signature proteins were determined based on the PAM with Canberra.

Phosphoproteomic data analysis. For the phosphoproteomic data, all the intensities of the phosphopeptides of 60 patient samples were exported from MaxQuant software (v1.6.1.0). The confidently identified phosphopeptides (with a 1% FDR and 75% localization probability) were normalized using the same strategy used for proteome analysis with the corresponding proteomic datasets. The in silico kinome activity profiling (iKAP) algorithm was applied to estimate kinase activity using the ratios of identified phosphosites with cutoff ratios of 1.45 between tumor and non-tumor tissues. iKAP estimates changes in a kinase's activity by calculating and summing all the identified substrates instead of only a single substrate, which could mitigate the bias from inherent noise of phosphoproteomics data (45). The estimation of kinase activities is based on the consensus phosphorylation motif of a kinase, while iGPS integrates publicly available databases such as PhosphoSite and Phospho.ELM to store information on all kinase-substrate networks and substrate motifs (95).

Correlations between mRNA and protein expression. To determine the correlations between the transcriptomic and proteomic data of ESCC patients, Spearman's correlation coefficients of genes/proteins were calculated using both RNA-Seq and MS data (5,676 genes) obtained from the tumor or paired non-tumor tissues. Additionally, gene set enrichment analysis (GSEA) was performed to identify pathway alterations. The GSEA scores were calculated based on the correlation scores obtained from tumor and non-tumor tissues (56).

Survival Curves. We utilized Kaplan-Meier analysis to estimate the OS of patients with different proteomic subtypes. The Cox proportional hazard model was used to evaluate the impact of protein expression on survival time. Prior to conducting the Log-rank test for a given protein, patients were classified into high and low groups based on their quantile-normalized protein levels in tumor tissues (< 1st quartile and > 3rd quartile, respectively). Subsequently, the corresponding Kaplan-Meier survival curves for OS were generated based on the cutoff point.

Potential prognostic biomarkers. The following four criteria were used to identify potential biomarkers: 1) candidate proteins were identified in all 60 tumor samples; 2) these candidate proteins exhibited high abundances, ranking among the top 1,000 proteins listed and displaying differential expression in tumor and adjacent non-tumor tissues; 3) the candidate proteins were highly expressed in the S-III subtype; and 4) highly expressed candidates were negatively correlated with OS (HR >1.5 and Kaplan-Meier analysis, Log-rank test, $P < 0.05$).

Immunohistochemistry. The human ESCC TMA (HEsoS180Su08) was obtained from Shanghai Outdo Biotech Company (Shanghai, China). Formalin-fixed, paraffin-embedded tumor and adjacent non-tumor samples were sectioned, deparaffinized, and hydrated. The TMA was subjected to antigen retrieval by boiling in sodium citrate buffer (10 mM/L, pH 6.0) for 90 seconds. Subsequently, the TMA was treated with 3% H_2O_2 for 5 minutes. Blocking was then performed using goat serum for 60 minutes before incubating overnight at 4°C with the specific primary antibody. The following day, the TMA was incubated with the secondary antibody for 30 minutes at room temperature (RT). Streptavidin working solution labeled with horseradish enzyme was applied to the TMA, which was then stained with DAB solution (ZSGB-

BIO, ZLI-9018); the reaction was terminated upon observation of color development under a microscope. Finally, counterstaining was conducted, and the data were analyzed by using Aperio Image Scope software (v12.3.2.8013).

Western blot. The cells or tissues were collected and treated with RIPA lysis buffer supplemented with protease and phosphatase inhibitors on ice. The lysate was gently pipetted to ensure complete cell lysis. Subsequently, the cell suspension was centrifuged at 14,000×g for 15 minutes at 4°C, and the resulting supernatant was transferred to a fresh tube. The protein concentration was determined using a BCA kit. The proteins were separated by SDS-PAGE and subsequently transferred onto PVDF membranes. Following the transfer, the membranes were blocked with 5% skim milk for 1 hour at RT. Next, the membrane was incubated with a specific primary antibody overnight at 4°C. The following day, the membranes were washed three times in TBST and then incubated with an HRP-conjugated secondary antibody for 2 hours at RT. Finally, after the membranes were washed three times with TBST, ECL reagent was added to visualize the specific bands.

shRNA. For gene knockdown, lentiviruses were generated by transfecting 293T cells with the shRNA plasmid, pMD2.G, and pSPAX2. The shRNA sequences cloned into the plasmids are provided in Supplemental Table 8. After transfection for 24 hours and 48 hours, the virus-enriched medium was collected, filtered through a 0.45 μm filter, and stored at 4°C for up to 1 week. Subsequently, ESCC cell lines were treated with lentivirus-enriched medium supplemented with polybrene (Sigma-Aldrich, TR-1003-G) for 24 hours. Afterward, the media was replaced with RPMI 1640 containing puromycin (Solarbio, P8230), and the cells were incubated for 1 to 2 days to select positive cells.

Overexpression. For gene overexpression, we constructed the overexpression plasmids PCDH-3×Flag-TIMMDC1 and PCDH-3×Flag-CSNK2A1. Transient transfection of the aforementioned plasmids was subsequently performed in the KYSE70 and KYSE150 cell lines. After 48 hours of transfection, the cells were harvested for Western blot analysis to evaluate the impact of overexpression.

Organoid culture. Esophageal PDX-derived organoids (PDXOs), derived from LEG334 and LEG352 ESCC PDX model tumors, were established using previously published protocols (96). The minced tumor tissue was incubated with buffer containing Y-27632 (MCE, HY-10071) and collagenase IV (Thermo, 17104019). Subsequently, the tissue fragments were filtered, and the collected cell suspension was centrifuged and resuspended in Matrigel (Corning, 356231) before being dispensed into the wells of a 24-well plate. Once the resuspended cells solidified, they were cultured in organoid medium (Thermo, 1234028) for 10-14 days. The cells were passaged at least three times for organoid formation.

For PDXO treatment, the organoid cells were transferred to a 96-well plate and cultured for 7 days. Images were acquired prior to and after CX-4945 treatment at concentrations ranging from 0 μM to 20 μM. After incubation for 96 hours, an MTT assay was performed, and the OD values at 570nm were obtained to assess the efficacy of CX-4945.

HDAC1 activity assay. The wild-type (WT) HDAC1 plasmid (PCDH-3×Flag-HDAC1) or mutant HDAC1 plasmids (PCDH-3×Flag-HDAC1 S421/S423D and PCDH-3×Flag-HDAC1 S421/S423A) were transfected into KYSE70 and KYSE 150 cells, respectively. Subsequently, the WT and mutant HDAC1 cells were harvested for quantification of HDAC activity using an HDAC1 colorimetric activity assay kit (GENMED, GMS50082.2). The calculation of HDAC1

activity was performed according to the manufacturer's recommendation.

In vitro kinase assay. For in vitro kinase assays, WT CSNK2A1 plasmid (PCDH-3×Flag-CSNK2A1) or mutant CSNK2A1 plasmids (PCDH-3×Flag-CSNK2A1 T360/S362D and PCDH-3×Flag-CSNK2A1 T360/S362A) were transfected into 293T cells. Subsequently, WT and mutant CSNK2A1 proteins were purified from 293T cells after 48 hours. Recombinant HDAC1 proteins were purified from E.coli. Subsequently, WT CSNK2A1 (100 ng) or mutant CSNK2A1 (100 ng) was incubated with 1 μg of recombinant WT HDAC1 protein and 250 μM ATP, respectively. The reactions were carried out in kinase buffer for 30 minutes at 30℃ and stopped by using a 6 × SDS sample buffer. Proteins were separated by SDS-PAGE and analyzed by Western blotting.

The methods used for the MTT, colony formation, and soft agar assays are described in the Supplemental methods.

Cell-derived xenograft (CDX). The CDX murine models were generated using the KYSE30 and KYSE450 cell lines. First, 6-week-old female Nu/Nu mice (SPF (Beijing) Biotechnology Co., Ltd.) were randomly divided into three groups: a scramble group, a sh1 group (shTIMMDC1 or shCSNK2A1 group), and a sh2 group (shTIMMDC1 or shCSNK2A1 group). For the KYSE30 cells, each group was subcutaneously injected with 5×10^6 stably transfected scramble cells, sh1 cells, or sh2 cells. Similarly, for the KYSE450 cells, three groups were subcutaneously injected with 1×10^7 stably transfected scramble cells, sh1 cells, or sh2 cells. Tumor volumes were measured twice weekly and calculated using the formula V = (length) × (width) × (width) / 2. Mice were euthanized when the tumor size reached approximately 1,000 mm^3. Tumor growth curves and tumor inhibition rates were calculated based on the recorded data.

Patient-derived xenograft (PDX). The LEG379, LEG397, and LEG460 cases were utilized to evaluate the effects of CX-4945 treatment. Approximately 0.08g of tumor tissue was implanted into 6-week-old female NOD-SCID mice (SPF (Beijing) Biotechnology Co., Ltd.) for each case. After one week, the NOD-SCID mice were separated into the control group, the 25 mg/kg group, and the 75 mg/kg group based on tumor volumes and body weights. CX-4945 was orally administered twice daily. Tumor volumes were assessed twice weekly utilizing the formula V = (length) × (width) × (width) / 2. Mice were euthanized when the tumor size reached approximately 1,000 mm^3. The tumor growth curves and tumor inhibition rates were calculated based on the recorded data.

The LEG244 case was utilized to assess the effect of lentivirus-mediated gene silencing. After the implantation of tumor fragments for one week, the mice were divided into three groups: the scramble group, the shCSNK2A1-1 group, and the shCSNK2A1-1 group. The lentivirus-enriched media were subjected to ultracentrifugation at 30,000 rpm for 3 hours at 4°C. Intratumoral injections of scramble virus, shCSNK2A1-1 virus, or shCSNK2A1-2 virus were administered twice weekly over a period of 6 weeks. Tumor growth curves and inhibition rates were calculated as indicated above.

Statistics. The following statistical analysis methods were utilized for single-omic and multi-omics data, experimental data, and clinical data. Standard two-sided statistical tests , including the Log-rank test, Student's *t* test, Fisher's exact test, Spearman's correlation, Wilcoxon test, Hypergeometric test, and ANOVA were used. To account for multiple-testing, adjusted P values were calculated using the Benjamini-Hochberg (BH) correction method. For experimental validation, each assay was repeated independently at least 3 times, the result presented as

mean ± SD. Statistical significance was determined by Student's *t* test and one-way ANOVA. Statistical significance is indicated by '*, $P < 0.05$; **, $P < 0.01$; ***, $P < 0.001$'.

Study approval. The use of clinical samples was received the approval of the Ethics Committee of China-US (Henan) Hormel Cancer Institute (No. CUHCIH2015001) and informed consent was obtained from all participants who volunteered for the study. The animal experiments conducted in this study were approved by the Ethics Committee of China-US (Henan) Hormel Cancer Institute (No. CUHCI2021002).

Data Availability. All original proteomic and phosphoproteomics data of this study were deposited to iProX (ProteomeXchange ID: PXD035562). All original of RNA-seq data of this study were deposited to SRA of NCBI (PRJNA861875). Analytic code for this study can be contact with the corresponding author. Values for all other data are available in the Supporting Data Values file.

Author Contributions

ZD and KL conceived and designed the study; DZ and YG developed methodology; YG and DZ performed software; YG, DZ, and WN performed formal analysis; GH, ZL, and JW provided resources; DZ, XJ, YZ, LH, and PW performed validation; DZ, HW, MHL, and KVL wrote original drafts; DZ and YG provided visualization; ZD and KL supervised the study; ZD, KL, and YG provided funding. The order of co-first authors was based on relevance of contributions to this project.

Acknowledgements

This work was supported by grants from the National Natural Science Foundation of China (grant nos. 81872335, 82073075, 32100532), the Central Plains Science and Technology Innovation Leading Talents (grant nos. 224200510015), the Supporting Plan of Zhengzhou University Youth Innovation Team (grant nos. 32320442), Joint Fund of the Scientific and Technical Research and Development Program of Henan (grant nos. 222301420056), and China Postdoctoral Science Foundation (grant nos. 2021M692936). We thank Dr. Fred Bogott (Austin Medical Center, Minnesota, USA) for helping us to modify the manuscript.

Address correspondence to: Kangdong Liu, Department of Pathophysiology, School of Basic Medical Sciences, Academy of Medical Science，Zhengzhou University, Zhengzhou, China. Phone: +86-0371-6778-1617. Email: kdliu@zzu.edu.cn (K.L.). Or to Zigang Dong, Department of Pathophysiology, School of Basic Medical Sciences, Academy of Medical Science, Zhengzhou University, Zhengzhou, China. Phone: +86-0371-6558-7008. Email: dongzg@zzu.edu.cn (Z.D.). Or to Mee-Hyun Lee, China-US (Henan) Hormel Cancer Institute, Zhengzhou, China. Phone: +82-61-330-3516 Email: mhyun_lee@hanmail.net (M.L.).

REFERENCES

1. Sung H, et al. Global Cancer Statistics 2020: GLOBOCAN Estimates of Incidence and Mortality Worldwide for 36 Cancers in 185 Countries. *CA Cancer J Clin.* 2021;71(3):209-49.
2. Bray F, et al. Global cancer statistics 2018: GLOBOCAN estimates of incidence and mortality worldwide for 36 cancers in 185 countries. *CA Cancer J Clin.* 2018;68(6):394-424.
3. Gao YB, et al. Genetic landscape of esophageal squamous cell carcinoma. *Nat Genet.* 2014;46(10):1097-102.
4. Yang YM, et al. Advances in targeted therapy for esophageal cancer. *Signal Transduct Target Ther.* 2020;5(1):229.
5. Li J, et al. Efficacy and safety of apatinib treatment for advanced esophageal squamous cell carcinoma. *Onco Targets Ther.* 2017;10:3965-9.
6. Gao Y, et al. Anlotinib as a molecular targeted therapy for tumors. *Oncology letters.* 2020;20(2):1001-14.
7. Hecht JR, et al. Lapatinib in Combination With Capecitabine Plus Oxaliplatin in Human Epidermal Growth Factor Receptor 2-Positive Advanced or Metastatic Gastric, Esophageal, or Gastroesophageal Adenocarcinoma: TRIO-013/LOGiC--A Randomized Phase III Trial. *Journal of clinical oncology : official journal of the American Society of Clinical Oncology.* 2016;34(5):443-51.
8. Sun JM, et al. Pembrolizumab plus chemotherapy versus chemotherapy alone for first-line treatment of advanced oesophageal cancer (KEYNOTE-590): a randomised, placebo-controlled, phase 3 study. *Lancet.* 2021;398(10302):759-71.
9. Wang X, et al. Lactate dehydrogenase and baseline markers associated with clinical outcomes

of advanced esophageal squamous cell carcinoma patients treated with camrelizumab (SHR-1210), a novel anti-PD-1 antibody. *Thorac Cancer.* 2019;10(6):1395-401.

10. Wang ZX, et al. Toripalimab plus chemotherapy in treatment-naive, advanced esophageal squamous cell carcinoma (JUPITER-06): A multi-center phase 3 trial. *Cancer Cell.* 2022;40(3):277-88 e3.

11. Lin DC, et al. Genomic and Epigenomic Aberrations in Esophageal Squamous Cell Carcinoma and Implications for Patients. *Gastroenterology.* 2018;154(2):374-89.

12. Song Y, et al. Identification of genomic alterations in oesophageal squamous cell cancer. *Nature.* 2014;509(7498):91-5.

13. Cui Y, et al. Whole-genome sequencing of 508 patients identifies key molecular features associated with poor prognosis in esophageal squamous cell carcinoma. *Cell Res.* 2020;30(10):902-13.

14. Mertins P, et al. Proteogenomics connects somatic mutations to signalling in breast cancer. *Nature.* 2016;534(7605):55-62.

15. Zhang H, et al. Integrated Proteogenomic Characterization of Human High-Grade Serous Ovarian Cancer. *Cell.* 2016;166(3):755-65.

16. Drake JM, et al. Phosphoproteome Integration Reveals Patient-Specific Networks in Prostate Cancer. *Cell.* 2016;166(4):1041-54.

17. Babu N, et al. Phosphoproteomic analysis identifies CLK1 as a novel therapeutic target in gastric cancer. *Gastric Cancer.* 2020.

18. Gao Q, et al. Integrated Proteogenomic Characterization of HBV-Related Hepatocellular Carcinoma. *Cell.* 2019;179(2):561-77 e22.

19. Chen YJ, et al. Proteogenomics of Non-smoking Lung Cancer in East Asia Delineates Molecular Signatures of Pathogenesis and Progression. *Cell.* 2020;182(1):226-44.e17.

20. Liu W, et al. Large-scale and high-resolution mass spectrometry-based proteomics profiling defines molecular subtypes of esophageal cancer for therapeutic targeting. *Nature communications.* 2021;12(1):4961.

21. Li Y, et al. Phosphoproteomics reveals therapeutic targets of esophageal squamous cell carcinoma. *Signal Transduct Target Ther.* 2021;6(1):381.

22. Salazar N, et al. A Chimeric Antibody against ACKR3/CXCR7 in Combination with TMZ Activates Immune Responses and Extends Survival in Mouse GBM Models. *Mol Ther.* 2018;26(5):1354-65.

23. Shi W, et al. COL11A1 as an novel biomarker for breast cancer with machine learning and immunohistochemistry validation. *Front Immunol.* 2022;13:937125.

24. Pan H, et al. Carboxypeptidase A4 promotes cell growth via activating STAT3 and ERK signaling pathways and predicts a poor prognosis in colorectal cancer. *Int J Biol Macromol.* 2019;138:125-34.

25. Sun S, et al. MiR-302b Suppresses Tumor Metastasis by Targeting Frizzled 6 in OSCC. *J Dent Res.* 2021;100(7):739-45.

26. Salazar N, et al. The chemokine receptor CXCR7 interacts with EGFR to promote breast cancer cell proliferation. *Mol Cancer.* 2014;13:198.

27. Duan Y, et al. CHAF1B promotes proliferation and reduces apoptosis in 95‐D lung cancer cells and predicts a poor prognosis in non‐small cell lung cancer. *Oncol Rep.* 2019;41(4):2518-28.

28. Yang X, et al. RNF126 as a Biomarker of a Poor Prognosis in Invasive Breast Cancer and CHEK1

Inhibitor Efficacy in Breast Cancer Cells. *Clin Cancer Res.* 2018;24(7):1629-43.

29. Ma G, et al. Circ-0005105 activates COL11A1 by targeting miR-20a-3p to promote pancreatic ductal adenocarcinoma progression. *Cell Death Dis.* 2021;12(7):656.

30. Chen J, et al. Expression of carbonic anhydrase 9 at the invasion front of gastric cancers. *Gut.* 2005;54(7):920-7.

31. Peng X, et al. CHAF1B knockdown blocks migration in a hepatocellular carcinoma model. *Oncol Rep.* 2018;40(1):405-13.

32. Hubackova S, et al. Replication and ribosomal stress induced by targeting pyrimidine synthesis and cellular checkpoints suppress p53-deficient tumors. *Cell Death Dis.* 2020;11(2):110.

33. Hu YC, et al. Profiling of differentially expressed cancer-related genes in esophageal squamous cell carcinoma (ESCC) using human cancer cDNA arrays: overexpression of oncogene MET correlates with tumor differentiation in ESCC. *Clinical cancer research : an official journal of the American Association for Cancer Research.* 2001;7(11):3519-25.

34. Chen Z, et al. Tissue-based metabolomics reveals metabolic biomarkers and potential therapeutic targets for esophageal squamous cell carcinoma. *J Pharm Biomed Anal.* 2021;197:113937.

35. Luo ML, et al. Amplification and overexpression of CTTN (EMS1) contribute to the metastasis of esophageal squamous cell carcinoma by promoting cell migration and anoikis resistance. *Cancer Res.* 2006;66(24):11690-9.

36. Kashyap MK, et al. Expression, regulation and targeting of receptor tyrosine kinases in esophageal squamous cell carcinoma. *Molecular cancer.* 2018;17(1):54.

37. Jiang YY, et al. TP63, SOX2, and KLF5 Establish a Core Regulatory Circuitry That Controls

Epigenetic and Transcription Patterns in Esophageal Squamous Cell Carcinoma Cell Lines. *Gastroenterology.* 2020;159(4):1311-27.e19.

38. Zhao Y, et al. PRMT1 regulates the tumour-initiating properties of esophageal squamous cell carcinoma through histone H4 arginine methylation coupled with transcriptional activation. *Cell Death Dis.* 2019;10(5):359.

39. Wang G, et al. A Comprehensive Analysis of Alterations in DNA Damage Repair Pathways Reveals a Potential Way to Enhance the Radio-Sensitivity of Esophageal Squamous Cell Cancer. *Frontiers in oncology.* 2020;10:575711.

40. Andrews B, et al. Assembly factors for the membrane arm of human complex I. *Proc Natl Acad Sci U S A.* 2013;110(47):18934-9.

41. Wang T, et al. C9orf72 regulates energy homeostasis by stabilizing mitochondrial complex I assembly. *Cell Metab.* 2021;33(3):531-46 e9.

42. Liu Y, et al. TIMMDC1 Knockdown Inhibits Growth and Metastasis of Gastric Cancer Cells through Metabolic Inhibition and AKT/GSK3beta/beta-Catenin Signaling Pathway. *Int J Biol Sci.* 2018;14(10):1256-67.

43. von Morgen P, et al. Nuclear localisation of 53BP1 is regulated by phosphorylation of the nuclear localisation signal. *Biol Cell.* 2018;110(6):137-46.

44. Shin YJ, et al. Protein kinase CK2 phosphorylates and activates p21-activated kinase 1. *Mol Biol Cell.* 2013;24(18):2990-9.

45. Chen LL, et al. Phosphoproteome-based kinase activity profiling reveals the critical role of MAP2K2 and PLK1 in neuronal autophagy. *Autophagy.* 2017;13(11):1969-80.

46. Liu TT, et al. Co-targeting PLK1 and mTOR induces synergistic inhibitory effects against

esophageal squamous cell carcinoma. *Journal of molecular medicine (Berlin, Germany).* 2018;96(8):807-17.

47. Jiang YY, et al. Targeting super-enhancer-associated oncogenes in oesophageal squamous cell carcinoma. *Gut.* 2017;66(8):1358-68.

48. Pinna LA. Protein kinase CK2: a challenge to canons. *J Cell Sci.* 2002;115(Pt 20):3873-8.

49. Kim JS, et al. Protein Kinase CK2α as an Unfavorable Prognostic Marker and Novel Therapeutic Target in Acute Myeloid Leukemia. *Clinical Cancer Research.* 2007;13(3):1019-28.

50. Pflum MK, et al. Histone deacetylase 1 phosphorylation promotes enzymatic activity and complex formation. *J Biol Chem.* 2001;276(50):47733-41.

51. Luo Y, et al. Serum insulin-like growth factor binding protein-3 as a potential biomarker for diagnosis and prognosis of oesophageal squamous cell carcinoma. *Ann Med.* 2022;54(1):2153-66.

52. Shou JZ, et al. Overexpression of CDC25B and LAMC2 mRNA and protein in esophageal squamous cell carcinomas and premalignant lesions in subjects from a high-risk population in China. *Cancer Epidemiol Biomarkers Prev.* 2008;17(6):1424-35.

53. Tang WW, et al. Upregulation of MAGEA4 correlates with poor prognosis in patients with early stage of esophageal squamous cell carcinoma. *Onco Targets Ther.* 2016;9:4289-93.

54. D'Amore C, et al. Role of CK2 inhibitor CX-4945 in anti-cancer combination therapy - potential clinical relevance. *Cell Oncol (Dordr).* 2020;43(6):1003-16.

55. Jin X, et al. A multi-omics study delineates new molecular features and therapeutic targets for esophageal squamous cell carcinoma. *Clin Transl Med.* 2021;11(9):e538.

56. Clark DJ, et al. Integrated Proteogenomic Characterization of Clear Cell Renal Cell Carcinoma.

Cell. 2019;179(4):964-83 e31.

57. Gillette MA, et al. Proteogenomic Characterization Reveals Therapeutic Vulnerabilities in Lung Adenocarcinoma. *Cell.* 2020;182(1):200-25 e35.

58. Mun DG, et al. Proteogenomic Characterization of Human Early-Onset Gastric Cancer. *Cancer Cell.* 2019;35(1):111-24 e10.

59. Zhang B, et al. Proteogenomic characterization of human colon and rectal cancer. *Nature.* 2014;513(7518):382-7.

60. Huang C, et al. Proteogenomic insights into the biology and treatment of HPV-negative head and neck squamous cell carcinoma. *Cancer Cell.* 2021;39(3):361-79 e16.

61. Xu JY, et al. Integrative Proteomic Characterization of Human Lung Adenocarcinoma. *Cell.* 2020;182(1):245-61 e17.

62. Ge S, et al. A proteomic landscape of diffuse-type gastric cancer. *Nat Commun.* 2018;9(1):1012.

63. Gujral TS, et al. A noncanonical Frizzled2 pathway regulates epithelial-mesenchymal transition and metastasis. *Cell.* 2014;159(4):844-56.

64. Tian R, et al. Identification and validation of the role of matrix metalloproteinase-1 in cervical cancer. *Int J Oncol.* 2018;52(4):1198-208.

65. Zhu Y, et al. MMP2/3 promote the growth and migration of laryngeal squamous cell carcinoma via PI3K/Akt-NF-kappaB-mediated epithelial-mesenchymal transformation. *J Cell Physiol.* 2019.

66. Pei YF, et al. Silencing of LAMC2 Reverses Epithelial-Mesenchymal Transition and Inhibits Angiogenesis in Cholangiocarcinoma via Inactivation of the Epidermal Growth Factor Receptor Signaling Pathway. *Am J Pathol.* 2019;189(8):1637-53.

67. Liang H, et al. A PTAL-miR-101-FN1 Axis Promotes EMT and Invasion-Metastasis in Serous

Ovarian Cancer. *Mol Ther Oncolytics.* 2020;16:53-62.

68. Zhu H, et al. Collagen stiffness promoted non-muscle-invasive bladder cancer progression to muscle-invasive bladder cancer. *Onco Targets Ther.* 2019;12:3441-57.

69. Wang T, et al. TOP2A promotes proliferation and metastasis of hepatocellular carcinoma regulated by miR-144-3p. *J Cancer.* 2022;13(2):589-601.

70. Zheng Y, et al. GTSE1, CDC20, PCNA, and MCM6 Synergistically Affect Regulations in Cell Cycle and Indicate Poor Prognosis in Liver Cancer. *Anal Cell Pathol (Amst).* 2019;2019:1038069.

71. Simonetti G, et al. Aneuploid acute myeloid leukemia exhibits a signature of genomic alterations in the cell cycle and protein degradation machinery. *Cancer.* 2019;125(5):712-25.

72. Satpathy S, et al. A proteogenomic portrait of lung squamous cell carcinoma. *Cell.* 2021;184(16):4348-71 e40.

73. Stewart PA, et al. Proteogenomic landscape of squamous cell lung cancer. *Nature communications.* 2019;10(1):3578.

74. Jiang Y, et al. Proteomics identifies new therapeutic targets of early-stage hepatocellular carcinoma. *Nature.* 2019;567(7747):257-61.

75. Law HC, et al. The Proteomic Landscape of Pancreatic Ductal Adenocarcinoma Liver Metastases Identifies Molecular Subtypes and Associations with Clinical Response. *Clinical cancer research : an official journal of the American Association for Cancer Research.* 2020;26(5):1065-76.

76. Li C, et al. Integrated Omics of Metastatic Colorectal Cancer. *Cancer Cell.* 2020;38(5):734-47 e9.

77. Djomehri SI, et al. Quantitative proteomic landscape of metaplastic breast carcinoma pathological subtypes and their relationship to triple-negative tumors. *Nature communications.* 2020;11(1):1723.

78. Liu M, et al. Molecular analysis of Chinese oesophageal squamous cell carcinoma identifies novel subtypes associated with distinct clinical outcomes. *EBioMedicine.* 2020;57:102831.

79. Wang F, et al. Gene Expression Profiling Reveals Distinct Molecular Subtypes of Esophageal Squamous Cell Carcinoma in Asian Populations. *Neoplasia.* 2019;21(6):571-81.

80. Wishart DS, et al. DrugBank 5.0: a major update to the DrugBank database for 2018. *Nucleic acids research.* 2018;46(D1):D1074-d82.

81. Guarani V, et al. TIMMDC1/C3orf1 functions as a membrane-embedded mitochondrial complex I assembly factor through association with the MCIA complex. *Mol Cell Biol.* 2014;34(5):847-61.

82. Wu H, et al. Depletion of C3orf1/TIMMDC1 inhibits migration and proliferation in 95D lung carcinoma cells. *Int J Mol Sci.* 2014;15(11):20555-71.

83. Birsoy K, et al. Untuning the tumor metabolic machine: Targeting cancer metabolism: a bedside lesson. *Nat Med.* 2012;18(7):1022-3.

84. Wheaton WW, et al. Metformin inhibits mitochondrial complex I of cancer cells to reduce tumorigenesis. *Elife.* 2014;3:e02242.

85. Bae JS, et al. CK2alpha/CSNK2A1 Phosphorylates SIRT6 and Is Involved in the Progression of Breast Carcinoma and Predicts Shorter Survival of Diagnosed Patients. *Am J Pathol.* 2016;186(12):3297-315.

86. Xie ZC, et al. A meta-analysis and bioinformatics exploration of the diagnostic value and molecular mechanism of miR-193a-5p in lung cancer. *Oncol Lett.* 2018;16(4):4114-28.

87. Rabjerg M, et al. Nuclear localization of the CK2alpha-subunit correlates with poor prognosis in clear cell renal cell carcinoma. *Oncotarget.* 2017;8(1):1613-27.

88. Slattery ML, et al. The NF-kappaB signalling pathway in colorectal cancer: associations between dysregulated gene and miRNA expression. *J Cancer Res Clin Oncol.* 2018;144(2):269-83.

89. Laramas M, et al. Nuclear localization of protein kinase CK2 catalytic subunit (CK2alpha) is associated with poor prognostic factors in human prostate cancer. *Eur J Cancer.* 2007;43(5):928-34.

90. Jiang C, et al. CSNK2A1 Promotes Gastric Cancer Invasion Through the PI3K-Akt-mTOR Signaling Pathway. *Cancer Manag Res.* 2019;11:10135-43.

91. Lou N, et al. Identification of novel serological autoantibodies in Chinese prostate cancer patients using high-throughput protein arrays. *Cancer Immunology, Immunotherapy.* 2022;72(1):235-47.

92. Tsuta K, et al. Utility of 10 immunohistochemical markers including novel markers (desmocollin-3, glypican 3, S100A2, S100A7, and Sox-2) for differential diagnosis of squamous cell carcinoma from adenocarcinoma of the Lung. *Journal of thoracic oncology : official publication of the International Association for the Study of Lung Cancer.* 2011;6(7):1190-9.

93. Cui T, et al. DSC3 expression is regulated by p53, and methylation of DSC3 DNA is a prognostic marker in human colorectal cancer. *British journal of cancer.* 2011;104(6):1013-9.

94. Barbie DA, et al. Systematic RNA interference reveals that oncogenic KRAS-driven cancers require TBK1. *Nature.* 2009;462(7269):108-12.

95. Song C, et al. Systematic analysis of protein phosphorylation networks from phosphoproteomic data. *Mol Cell Proteomics.* 2012;11(10):1070-83.

96. Karakasheva TA, et al. Generation and Characterization of Patient-Derived Head and Neck, Oral, and Esophageal Cancer Organoids. *Curr Protoc Stem Cell Biol.* 2020;53(1):e109.

Figures

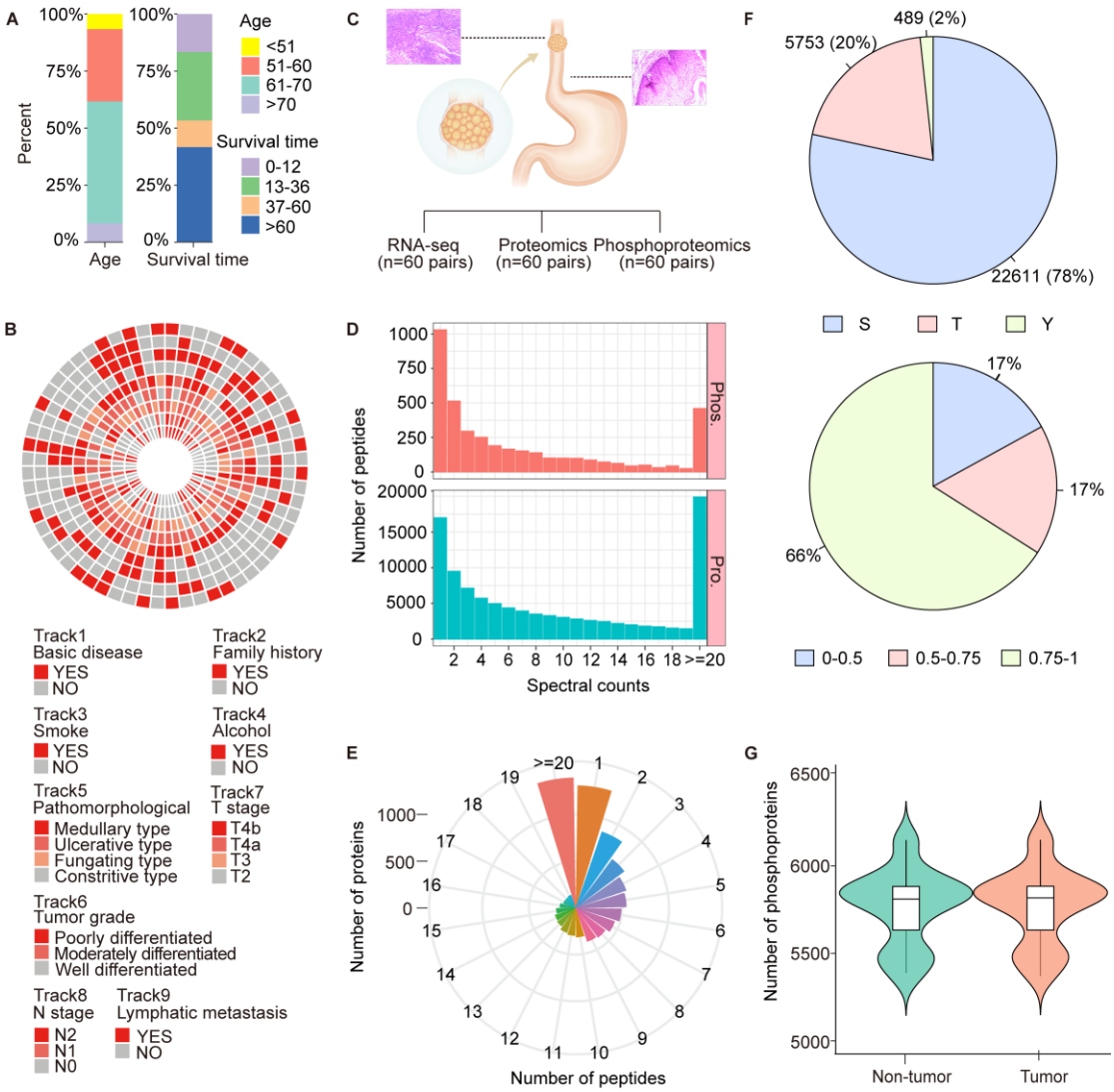

Figure 1. Summary of RNA-seq, proteomics, and phosphoproteomics analysis in ESCC. (**A**) Stacked histograms depicting the distribution of age and survival time of 60 patients. Statistical unit for age: year; statistical unit for survival time: month. (**B**) Circular heatmap illustrating the distribution of clinical information among 60 ESCC patients. Each axis represents an individual patient, and each track represents corresponding patient information. (**C**) Schematic illustrating the flowchart of this study. (**D**) Histograms illustrating the raw LC-MS/MS spectral counts distribution of peptides and phosphopeptides identified from proteomics and phosphoproteomics data, respectively. Pro.: proteomics, Phos.: phosphoproteomics. (**E**) Circular bar plot displaying the peptide numbers distribution identified from proteomics data. (**F**) Pie charts presenting the composition of phosphorylated residue type (p-Ser, p-Thr, and p-Tyr) (top), as well as assigned localization probability (bottom) for all detected phosphosites. (**G**) Violin plot illustrating the number of quantified phosphoproteins in paired tumor and adjacent non-tumor tissues.

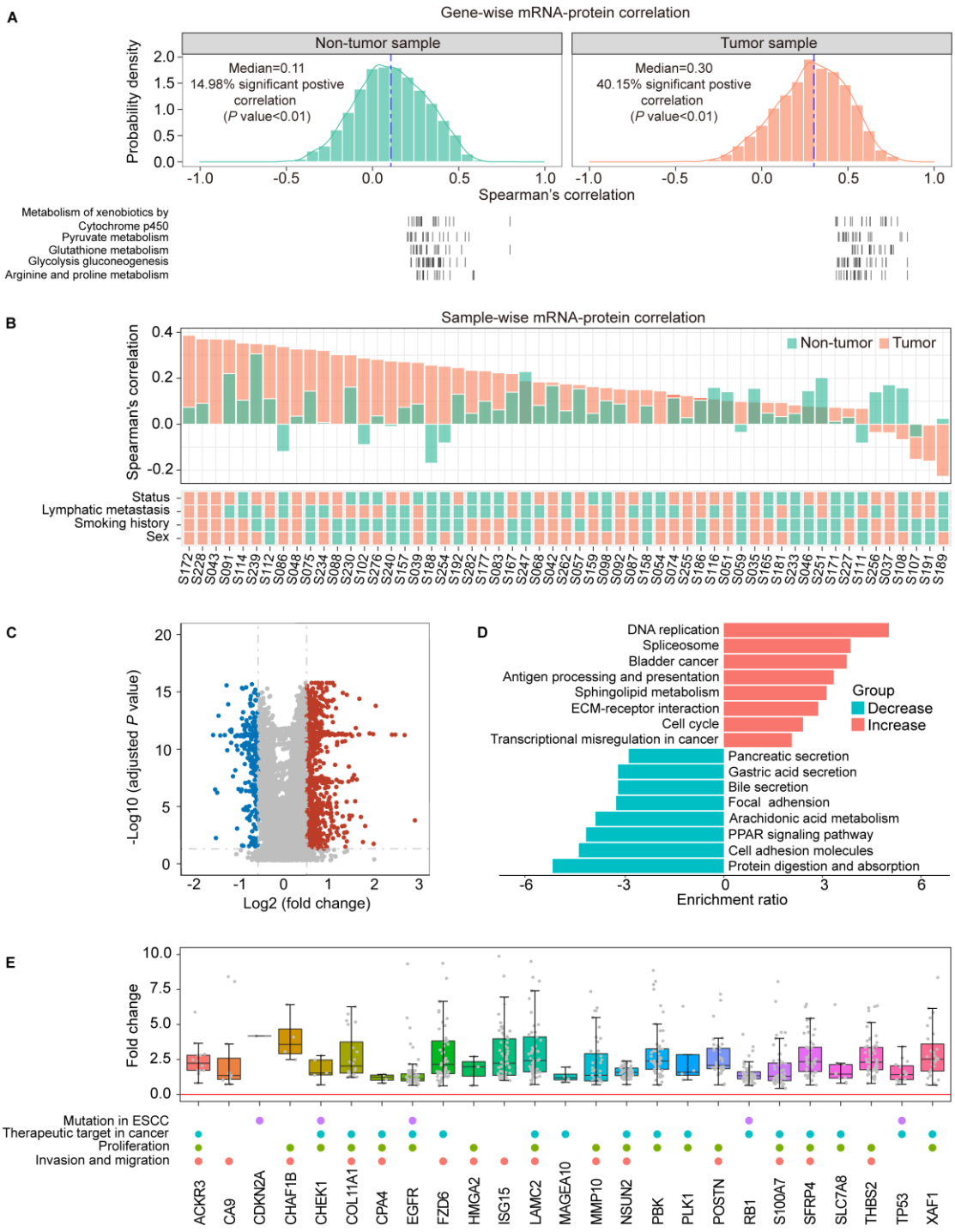

Figure 2. ESCC proteomic profiling in tumor and adjacent non-tumor samples. (**A**) Histogram illustrating the gene-wise correlations of mRNA and protein expression in adjacent non-tumor (left, n=60) and tumor tissues (right, n=57). The green color represents adjacent non-tumor tissue, and the red color represents tumor tissue. (**B**) Histogram illustrating the sample-wise correlations of adjacent non-tumor (n=57) and tumor tissues (n=57). The green color represents adjacent non-tumor tissue, and the red color represents tumor tissue. Living status, smoking history, lymphatic metastasis, and sex of each patient are listed directly below the histogram. Green color represents living patients, red color represents deceased patients; Green color represents no lymphatic metastasis, red color represents lymphatic metastasis; Green color represents non-smoking history, red color represents a smoking history; Green color represents female patients, red color represents male patients. (**C**) Volcano plot indicating differential proteins between

tumor and adjacent non-tumor tissues. Red dots represent upregulated proteins in tumor tissues compared to adjacent non-tumor tissues, while blue dots represent downregulated proteins. Gray dots represent proteins with no significant difference between tissues. (**D**) Enriched KEGG pathways of upregulated and downregulated proteins in tumor tissues compared to adjacent non-tumor tissues. (**E**) Histogram illustrating differential expression of representative proteins along with their mutation status, target potential, and cancer-related phenotypes such as proliferation, invasion, and migration.

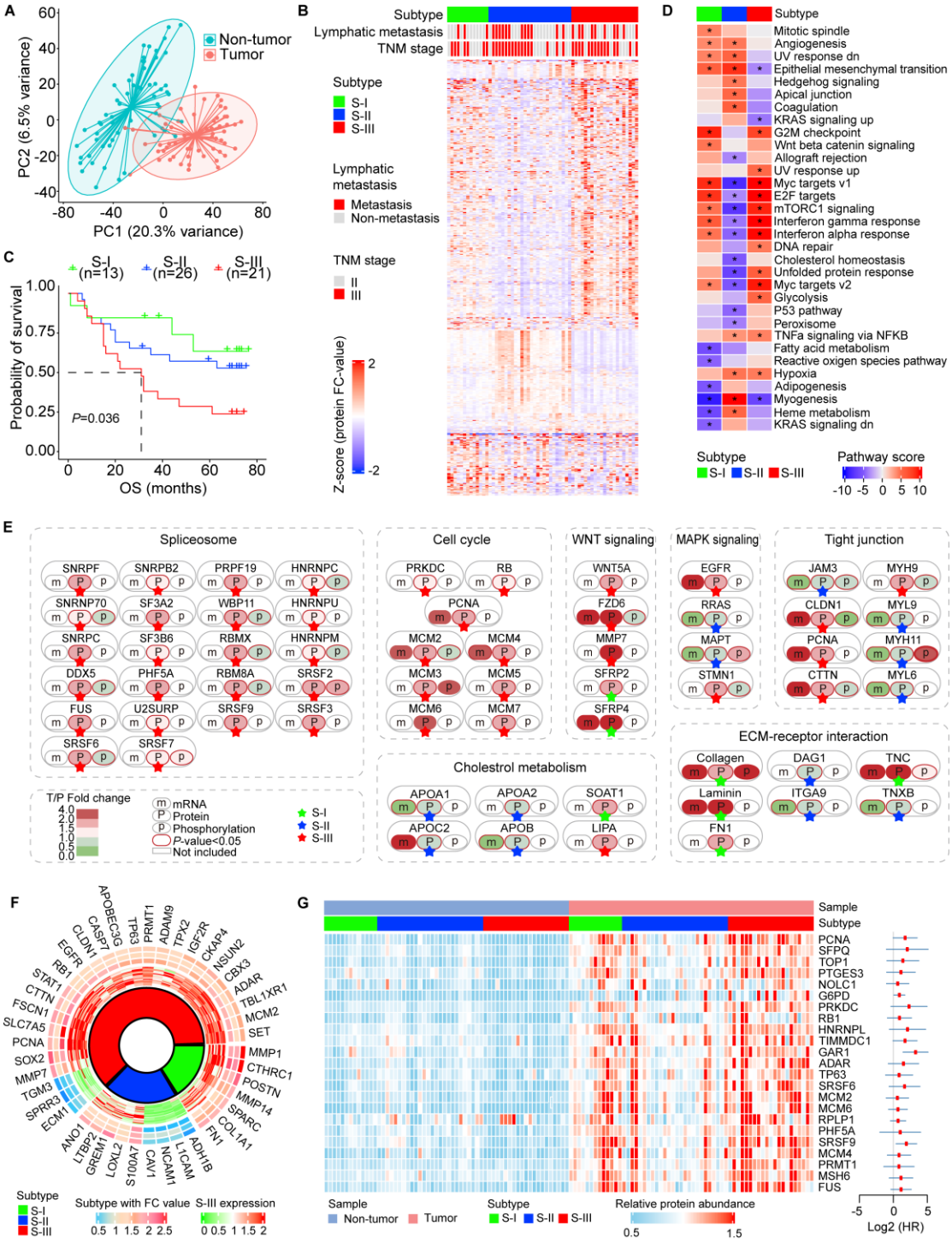

Figure 3. Molecular subtyping of ESCC. (**A**) PCA analysis of protein expression in tumor and adjacent non-tumor samples. The red oval represents tumor tissue, and the green oval represents adjacent non-tumor tissue. (**B**) Heatmap shows three consensus clusters based on the proteomics data, with their associations with clinical information such as lymphatic metastasis and TNM stages presented in the middle panel. (**C**) Kaplan-Meier plot comparing survival probability of patients in Subtypes I-III. (**D**) Heatmap elucidating the major signaling pathways enriched in Subtypes I-III. (**E**) Integrative molecular network analysis reveals the expression of mRNA, protein, and phosphoprotein for representative molecular of Subtypes I-III. (**F**) Circular heatmap displaying representative molecular characteristics of Subtypes I-III. (**G**) Expression levels and HRs for selected proteins in Subtype III.

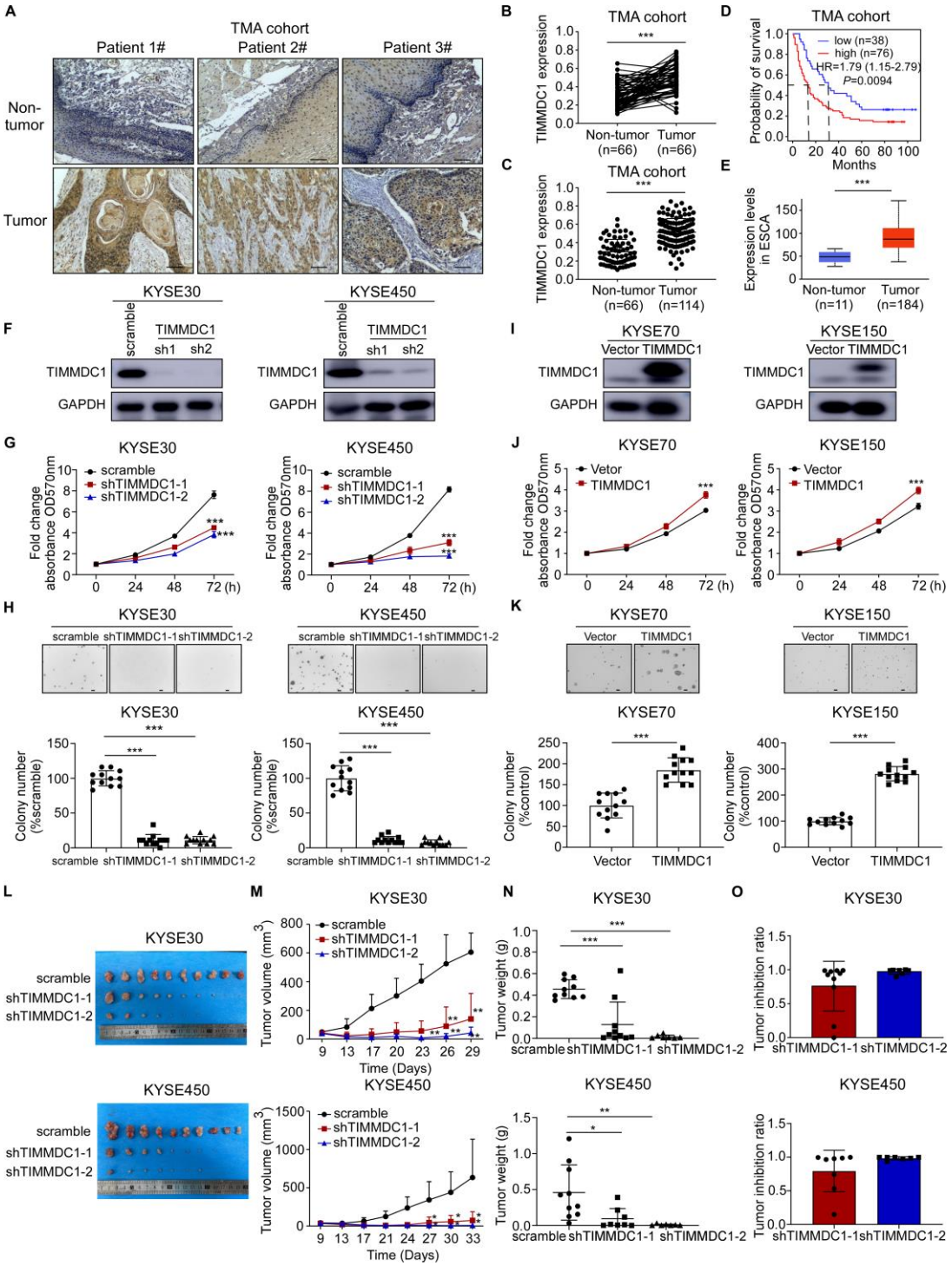

Figure 4. Elevated expression of TIMMDC1 promotes ESCC growth and is associated with poor prognosis. (**A**) Representative IHC staining images of a human ESCC TMA using a specific antibody for TIMMDC1 are shown. Scale bar: 100 μm. (**B-C**) Protein levels of TIMMDC1 were analyzed in an ESCC TMA, including paired tumor and adjacent non-tumor tissues of 66 patients (B), and tumors without paired non-tumor tissues for of patients (**C**). (**D**) Kaplan-Meier plot comparing the survival probability of patients with high/low TIMMDC1 expression. (**E**) Transcript expression level of TIMMDC1 was determined in the TCGA-ESCA patient cohort. (**F**) TIMMDC1 knockdown efficiency was assessed by Western blot. (**G-H**). Cell proliferation was measured by MTT (n=6 for each group) (**G**) and soft agar (n=12 for each group) assays (**H**) after knockdown of TIMMDC1. Scale bar: 200 μm. (**I**) TIMMDC1 overexpression efficiency was assessed by Western blot. (**J-K**) Cell proliferation was measured by MTT (n=6 for each group) (**J**) and soft agar (n=12

for each group) assays (**K**) after overexpression of TIMMDC1. Scale bar: 200 μm. (**L-O**) KYSE30 and KYSE450 cells stably expressing scramble or shTIMMDC1 were subcutaneously injected into the right flank of each mouse (KYSE30: scramble n=10; sh1 n=10; sh2 n=7; KYSE450: scramble n=10; sh1 n=8; sh2 n=7). Tumors were excised at the end of the experiment. (**L**) Images of xenograft tumors. (**M**) Xenograft tumor growth curves in mice. (**N**) Weights of xenograft tumors. (**O**) Tumor inhibition ratios of TIMMDC1 knockdown. In all statistical plots, data were expressed as the mean ± SD. Student's *t* test (B, C, E, J, and K) and one-way ANOVA analysis (G, H, M, and N) were used to determine statistical significance. $^{*}P < 0.05$, $^{**}P < 0.01$, $^{***}P < 0.001$. Representative results from at least 3 independent biological replicates (F-K) are shown.

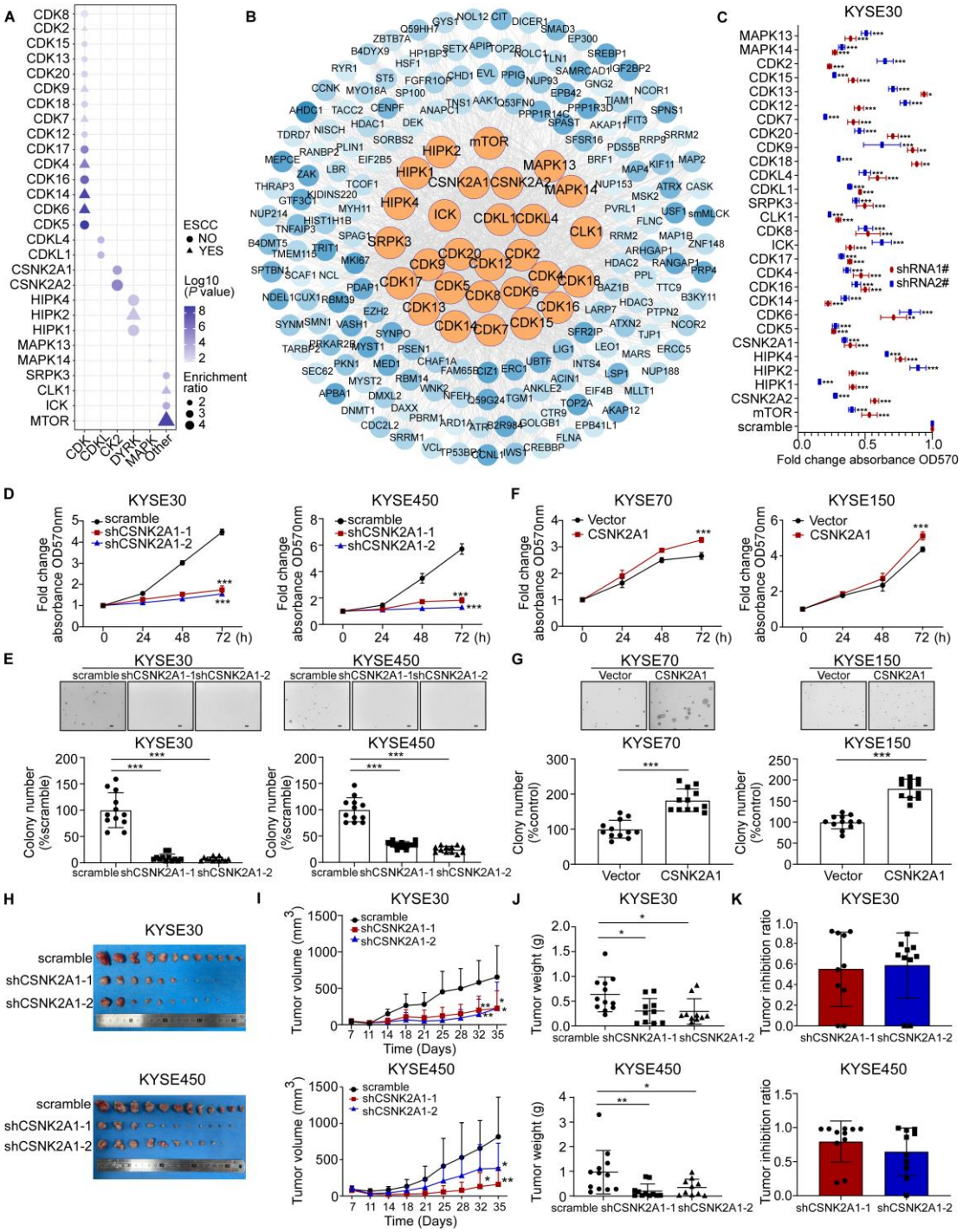

Figure 5. Identification of kinases and their potency in ESCC. (**A**) Potential activated kinases predicted by a kinase-substrate phosphorylation network are depicted. Dots represent previously unstudied kinases in ESCC, and triangles represent kinases implicated in ESCC based on previous literature. The color denotes the calculated P value for each kinase, and the size of the shapes corresponds to their enrichment ratios. (**B**) Kinase-phosphosubstrate regulation networks are depicted for selected kinases and their substrates, with orange circles representing kinases and blue circles representing their corresponding substrates. (**C**) Cell proliferation at 72 hours was evaluated by MTT assay after knockdown of the indicated kinases in KYSE30 cell (n=6 for each group). (**D-E**) Cell proliferation measured by MTT assay (n=6 for each group) (**D**) and soft agar assay (n=12 for each group) (**E**) after CSNK2A1 knockdown. Scale bar: 200 μm. (**F-G**) Cell proliferation measured by MTT (n=6 for each group) (**F**) and soft agar (n=12 for each group) (**G**) assays after CSNK2A1 overexpression. Scale bar: 200 μm. (**H-K**) KYSE30 and KYSE450 cells stably expressing

scramble or shCSNK2A1 were subcutaneously injected into the right flank of each mouse (KYSE30: scramble n=12; sh1 n=10; sh2 n=10; KYSE450: scramble n=12; sh1 n=11; sh2 n=10). Tumors were excised at the end of the experiment. Images of xenograft tumors are shown in (**H**), while (**I**) presents xenograft tumor growth curves data from mice experiments; (**J**) displays tumor weights; (**K**) represents tumor inhibition ratios. In all statistical plots, data were expressed as the mean ± SD. Student's *t* test (F, and G) and one-way ANOVA analysis (C-E, I, and J) were used to determine statistical significance. **P* < 0.05, ***P* < 0.01, ****P* < 0.001. Representative results from at least 3 independent biological replicates (C-G) are shown.

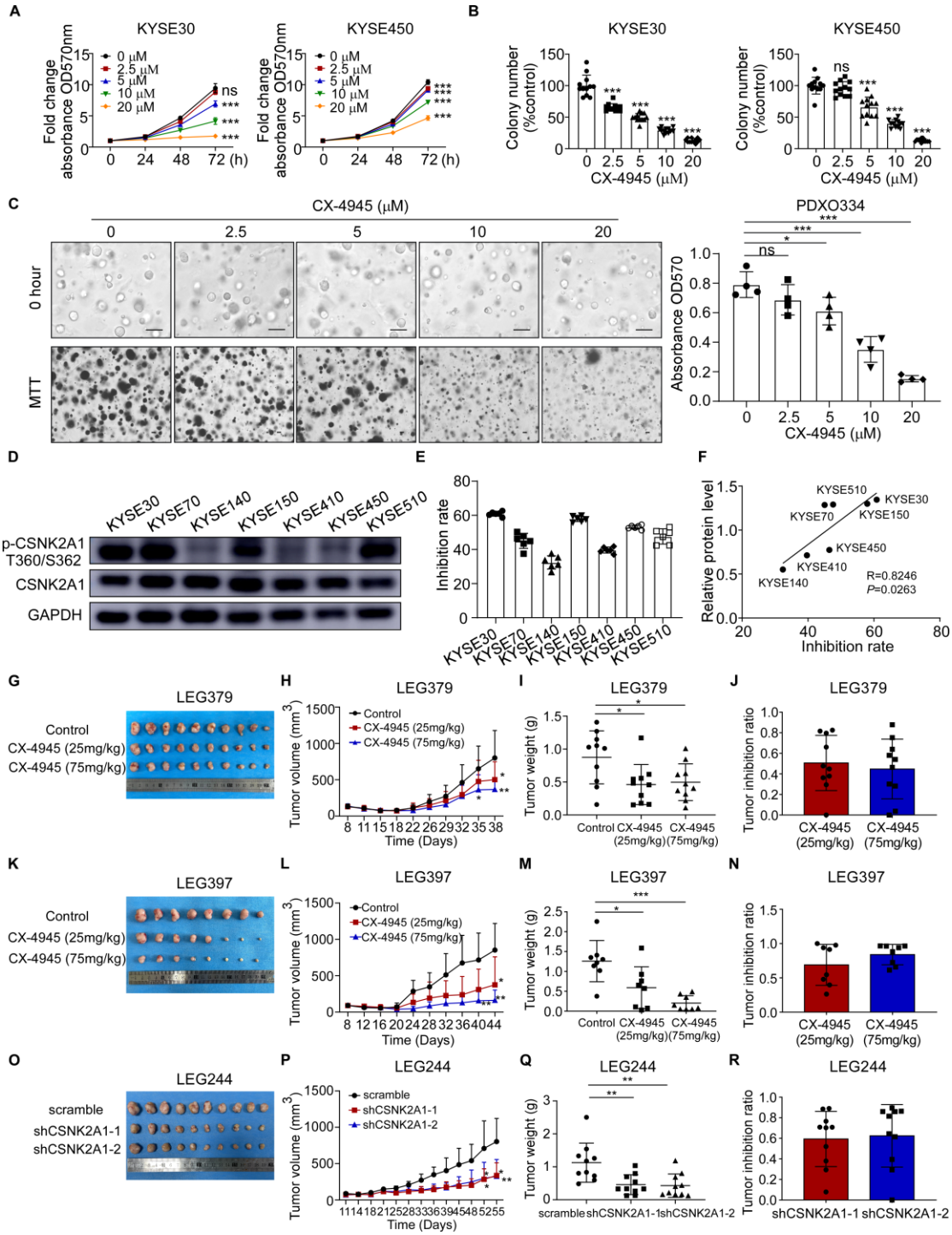

Figure 6. Tumor inhibitory effect of CX-4945 in vitro and in vivo. (**A-B**) MTT (n=6 for each group) (**A**) and soft agar (n=12 for each group) (**B**) assays were performed on KYSE30 and KYSE450 cells following treatment with CX-4945 at concentrations ranging from 0 μM to 20 μM. (**C**) The growth of organoids was evaluated after treatment with CX-4945 at the same concentration (n=4 for each group). Scale bar: 100 μm. (**D**) Western blotting was performed to determine the protein levels of CSNK2A1 and p-CSNK2A1 T360/S362 in ESCC cell lines. (**E**) The inhibitory effect of CX-4945 on cell proliferation was assessed using MTT assay in ESCC cell lines. (**F**) Pearson correlation analysis was employed to evaluate the correlation between p-CSNK2A1 T360/S362 levels and inhibition rate of cell proliferation in seven ESCC cell lines. (**G**) LEG379 tumors excised from the mice treated with CX-4945 were analyzed (n=10 for each group). (**H-J**) PDX tumor growth (**H**), tumor weights (**I**), and tumor inhibition ratios (**J**) of the LEG379 case treated with

CX-4945 were determined. Similarly, (**K**) LEG397 tumors excised from mice treated with CX-4945 were examined (n=8 for each group), followed by analysis of PDX tumor growth (**L**), tumor weights (**M**), and tumor inhibition ratios (**N**) of the LEG397 case. Additionally, LEG244 tumors obtained from mice treated with lentiviruses encoding shCSNK2A1 were investigated (n=10 for each group). (**O**). PDX Tumor growth (**P**), tumor weights (**Q**), and tumor inhibition ratios (**R**) of the LEG244 case treated with lentiviruses encoding shCSNK2A1 were determined. In all statistical plots, data were expressed as the mean ± SD. One-way ANOVA analysis (A-C, H, I, L, M, P, and Q) was used to determine statistical significance. *$P < 0.05$, **$P < 0.01$, ***$P < 0.001$. Representative results from at least 3 independent biological replicates (A-E) are shown.